Journal of Applied Fluid Mechanics, Vol. 18, No. 6, pp. 1617-1638, 2025.
Available online at www.jafmonline.net, ISSN 1735-3572, EISSN 1735-3645.
https://doi.org/10.47176/jafm.18.6.3084

Contribution of Suspension Bogies' Aerodynamic Loads to the Dynamic Characteristics of a High-temperature Superconducting Maglev Train Running under Crosswind

Z. P. Li[1,2], X. F. Wang[1,2], Y. M. Pan[1,2], Y. Ding[2], P. F. Liu[3] and Z. G. Deng[2†]

[1] *School of Mechanics and Aerospace Engineering, Southwest Jiaotong University, Chengdu 610031, China*
[2] *State Key Laboratory of Rail Transit Vehicle System, Southwest Jiaotong University, Chengdu 610031, China*
[3] *State Key Laboratory of Mechanical Behavior and System, Shijiazhuang Tiedao University, Shijiazhuang 050043, China*

†*Corresponding Author Email: deng@swjtu.cn*

ABSTRACT

The suspension bogies at the bottom of the high-temperature superconducting pinning (HTS) maglev trains are critical components, responsible for levitation, guidance, shock absorption, etc. This research delves into the aerodynamic load features of the suspension bogies on HTS maglev trains when operating under various crosswind conditions. By employing the unsteady Reynolds-averaged Navier-Stokes (URANS) equations coupled with the shear stress transport (SST) k-ω turbulence model, we elucidate the dynamic impact of these aerodynamic loads on the vehicle's overall performance, thereby offering valuable insights into the structural design of the train. The accuracy of the numerical method was confirmed by using wind tunnel test data from the scaled ICE-2 model. Furthermore, by adopting a strategy of partitioning the aerodynamic load, the impact on the overall vehicle dynamics performance is analyzed, and the operational safety of the train under different crosswind scenarios is assessed with Multi-body Dynamic (MBD) simulations. The research results indicate that the first bogie at the bottom of the head car contributes the most to the unsteady fluctuations of the aerodynamic load. Additionally, the partitioned loading method has a significant impact on the simulation results, which can better assess the safety of the train's operation under crosswinds. The research findings can provide references for the system design and engineering application of the HTS maglev train.

Article History

Received September 3, 2024
Revised December 22, 2024
Accepted January 6, 2025
Available online March 30, 2025

Keywords:

High-speed maglev train
Multi-body dynamic simulations
Crosswind
Aerodynamic loads
Computational fluid dynamics

1. Introduction

High-temperature superconducting (HTS) pinning magnetic levitation technique relies on the interaction between the permanent magnetic guideway (PMG) and the onboard superconducting components to provide levitation and guidance Sawada (2009). It has a straightforward construction and achieves self-stabilization without the need for an external power source Wang et al. (2007), and no magnetic resistance in the direction of motion Werfel et al. (2012), Hull (2000), which provides the capability for high-speed operation. Worldwide, researchers have created many experimental and technical prototypes of HTS maglev cars (Wang et al. 2003; Sotelo et al. 2015; Deng et al. 2016; Mattos et al. 2016). In 2021, an engineering prototype was introduced at Southwest Jiaotong University in Chengdu, China (Wang et al., 2021). This HTS high-speed train prototype, exceeding 15 tons, has a streamlined design and a high-thrust linear engine for enhanced velocity. The HTS maglev train's lower suspension bogies, which provide levitation and guidance functions, face direct aerodynamic forces and vibrations from the train body at elevated speeds. Examining these forces and their dynamic effects is essential for enhancing the design of the high-speed HTS maglev train.

Investigations on the aerodynamic efficacy of high-speed maglev trains in crosswinds may certainly reference findings from the high-speed rail industry (Tian, 2019; Ding et al. 2023). Early studies on high-speed trains operating in crosswinds mostly included full-scale vehicle testing and wind tunnel trials (Suzuki et al., 2003; Baker et al., 2004; Dorigatti et al., 2015). Due to advancements in numerical simulation methods, Computational Fluid Dynamics (CFD) has progressively supplanted wind tunnel testing for evaluating aerodynamic properties in

crosswinds. Baker (2009) examined the wake formation of a train subjected to wind using experimental data and numerical simulations. Zhang (2013) utilized a Large Eddy Simulation (LES) to investigate the unsteady aerodynamic loads on a high-speed train in crosswinds, demonstrating that the aerodynamic load on the train exhibits pronounced unsteady characteristics, and the selection of the simplified center influences the unsteady characteristics of aerodynamic torque. Munoz-Paniagua et al. (2017) evaluated the efficacy of three numerical models—Explicit Algebraic Reynolds Stress Model (EARSM), Scale Adaptive Simulation (SAS), and Improved Delayed Detached Eddy Simulation (IDDES)—in addressing aerodynamic challenges faced by high-speed trains in crosswind conditions. Zhang (2012) examined the dynamics of a 350 km/h high-speed train traversing a windbreak wall in crosswinds by CFD and dynamic modeling, proposing a buffered windbreak design to enhance crosswind aerodynamic safety. Wang et al. (2018) examined the aerodynamic properties of trains subjected to two varieties of crosswinds: uniform and exponential. Significant disparities were seen in the aerodynamic performance of trains simulated with these two wind types, with the leading car exhibiting the least safety under crosswind circumstances. Niu et al. (2018) examined the aerodynamic efficacy of the CRH2C high-speed train in static and dynamic models subjected to crosswinds, both with and without a windbreak wall. The results demonstrated that for trains equipped with a windbreak wall in crosswind conditions, the newly generated vortices near the train body, caused by the windbreak wall, are substantially affected by the train's motion, rendering the replacement of stationary train methods with moving train simulations unsuitable. High-speed maglev trains function at velocities beyond those of traditional high-speed trains and possess a minimal clearance between the vehicle's bottom and the track, which complicates its aerodynamic efficiency. Meng et al. (2022) examined the influence of non-smooth surfaces on the aerodynamics of maglev trains. Huang et al. (2024) examined the aerodynamic properties of high-speed maglev trains with different formation lengths in crosswind scenarios. Lin et al. (2024) investigated the impact of suspension gaps on the wake of superconducting maglev trains operating at velocities of 600 km/h. Han et al. (2022) investigated the impact of train velocity on pressure waves produced by maglev trains traversing tunnels.

Moreover, studies often correlate the aerodynamic efficiency and dynamic behavior of trains subjected to crosswinds. Tian et al. (2023) formulated a coupled dynamic model for high-speed maglev trains and track beams subjected to crosswind conditions, examining the effects of mean wind, gusts, wind velocity, and train speed on the dynamic response of the maglev system. Liu et al. (2011) and Yu (2012) used Large Eddy Simulation (LES) to examine the transient aerodynamic forces on trains subjected to crosswinds in both temporal and frequency domains. Krajnović et al. (2012) employed the Large Eddy Simulation (LES) method to study the aerodynamic characteristics of a simplified train model under crosswinds, both statically and dynamically, and compared the results with wind tunnel experiments. A Multi-Body Dynamics (MBD) model for high-speed trains was created, using computed forces to evaluate operating safety under these loads. Li et al. (2012) integrated vehicle dynamics with aerodynamic theory to develop a fluid-structure interaction simulation for high-speed trains, demonstrating that coupling effects significantly influence the aerodynamics and stability of the lead car. Zhang (2016) examined the unsteady aerodynamics and safety of trains subjected to crosswinds over various terrains, using train aerodynamics and vehicle dynamics. They delineated the temporal and spectral distributions of the primary aerodynamic loads, observing that these loads mostly occur below 5 Hz in frequency. Lv et al. (2023) investigated the aerodynamic braking properties of high-speed maglev trains traveling at 600 km/h under crosswind conditions and included the unsteady aerodynamic forces into the vehicle dynamics for study. Liu et al. (2022) examined the aerodynamic load contributions of bogies and analyzed the aerodynamic load characteristics and dynamic performance of high-speed trains under various crosswind conditions, taking wheelset rotation into account.

Current research primarily focuses on the aerodynamics, overturning hazards, and dynamic responses of high-speed rail trains, while insufficiently addressing the aerodynamic load contributions in the suspension bogies of maglev trains. Research on the performance of HTS maglev trains in crosswinds is limited; only Wang et al. (2023) examined the aerodynamics of HTS maglev trains in crosswinds at elevated speeds, assessing safety by including stable aerodynamic forces into the train's center of mass. Li et al. (2023) examined the dynamic properties of the HTS maglev train under crosswind situations.

The total aerodynamic load methodology in prior research neglects the transmission of vibrations via the secondary suspension between the bogies and the automobile body, together with the vibrations generated by aerodynamic loads on the bogies. The bogies at the base of the HTS maglev train are exposed to air and directly subjected to aerodynamic forces. The levitation and steering components on the bogie are similarly affected, thereby jeopardizing the train's operating safety. Therefore, more emphasis is necessary on the impact of aerodynamic forces from each bogie on the dynamic response and operational safety of the HTS maglev train. This work use CFD simulations to examine the aerodynamic loads on each vehicle component, integrating the partitioned independent loading approach with MBD simulations to assess the aforementioned projects.

This paper is structured as follows: Section 1 delineates the history, present research status, and principal focal areas concerning the aerodynamic properties and safety analyses of high-speed trains in crosswind conditions. Section 2 delineates the scenarios and specifies the model particulars of this investigation. Section 3 presents numerical models, including the CFD computational domain, the used grids and numerical methods, the validation of CFD simulations, and the development of an

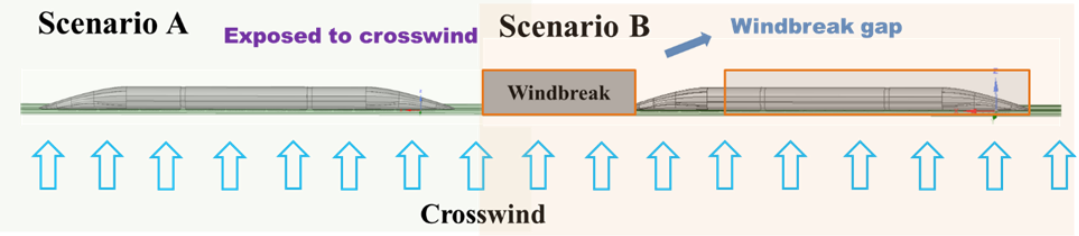

Fig. 1 Schematic view of the two crosswind scenarios studied in this study

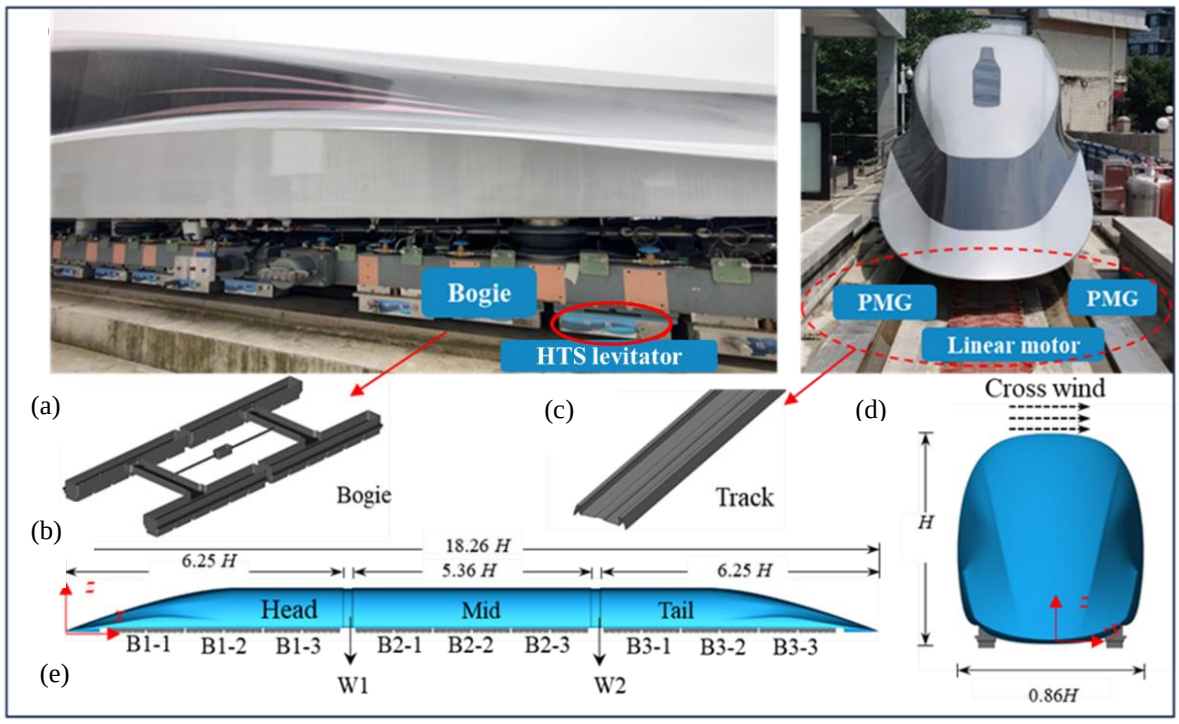

Fig. 2 Model and key components of the HTS maglev train: (a) the prototype of the HTS maglev head vehicle in Southwest Jiaotong University, (b) the suspension bogie of the HTS maglev train, (c) the track of the maglev line, (d) the front view and key dimensions of the HTS maglev train, (e) side view and key dimensions of the HTS maglev train

MBD model. Section 4 delineates and analyzes the outcomes of CFD computations, the dynamic responses, and safety metrics. The main results drawn from the research are presented in Section 5.

2. SCENARIOS AND GEOMETRY MODEL

Referencing Liu et al. (2022) and considering the layout and environmental wind conditions of Chinese high-speed railways, we classify the running scenarios of HTS maglev trains in crosswinds into two categories (Scenario A and Scenario B), as illustrated in Fig.1. The first type consists of high-speed maglev trains operating entirely in an open-line environment, where the vehicles are fully exposed to crosswind loads. The second type delineates a scenario in which high-speed maglev trains are progressively subjected to crosswinds. This scenario is relevant due to the significance of crosswind speed and direction in influencing train operation safety; these fluctuations in crosswind loads are referred to as wind shear. Instances include trains traversing openings in windbreak structures or entering and exiting tunnels, during which they encounter differing crosswind forces. Figure 2 presents the full-scale model of a three-car HTS maglev train utilized in this study, which is derived from the prototype of the HTS maglev head vehicle (Fig. 2 (a)). The model incorporates features such as the windshield ($W1$ and $W2$) and the suspension bogies (Fig.2 (a) and (b)), utilizing HTS levitators—heat-insulation devices containing liquid nitrogen and HTS bulks—to generate levitation and guidance forces, as illustrated in Fig.2 (a). Additionally, it includes the U-shaped track, linear motor, and permanent magnet guideway (PMG) of the maglev line. Figures 2 (c), (d), and (e) illustrate the front and side views of the train model. The train possesses a height of H (H = 3.36 m) and an overall length of approximately 18.26 H (61.36 m), with a width of about 0.863 H (2.90 m). Each car body is equipped with three suspension bogies, resulting in a total of nine bogies for the entire train. These bogies are sequentially numbered from the head car to the tail car as B1-1, B1-2, B1-3; B2-1, B2-2, B2-3; B3-1, B3-2, B3-3.

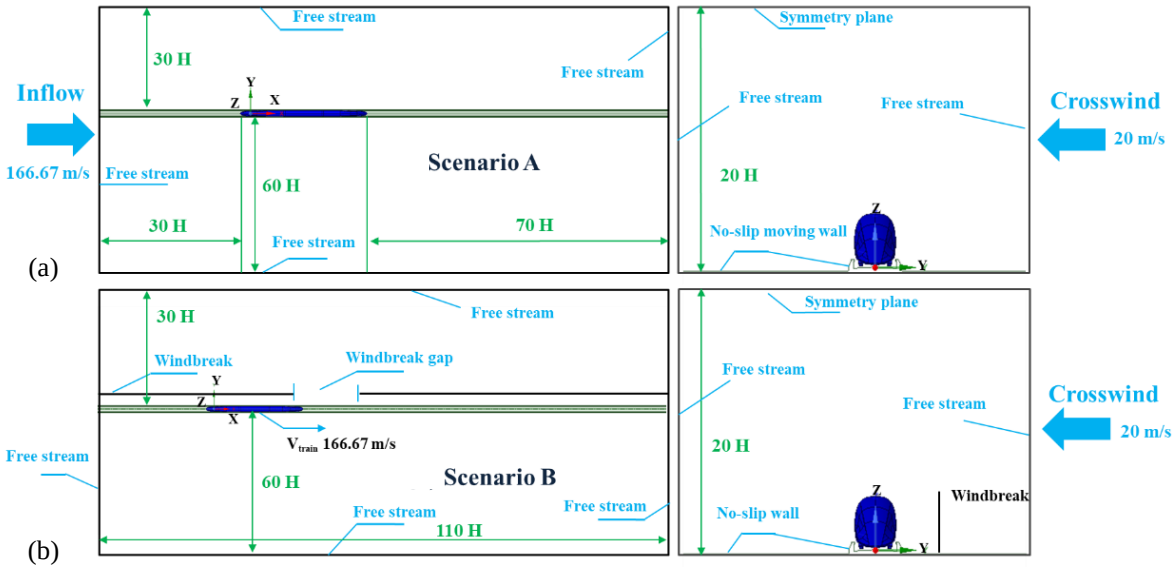

Fig. 3 Computational domain and boundary conditions for Scenarios A and B

3. NUMERICAL MODELS

3.1 Computational Domain and Boundary Conditions

This paper establishes a computational domain with dimensions illustrated in Fig.3. In Scenario A, the domain measures 110 H (370 m) in length, 20 H (67 m) in height, and 90 H (300 m) in width. The train remains stationary within the computational domain, while the track and ground move at a speed of -V_{train} (600 km/h) in the opposite direction of the train. The incoming flow velocity U is the vector sum of the train speed and the crosswind speed V_{wind}, which is 20 m/s. The crosswind direction angle α refers to the angle formed between the wind direction and the direction of the train's travel. This paper establishes that the wind direction is oriented along the negative *y-axis*, corresponding to a wind direction angle of 90°. The composite wind direction angle β is defined as the angle formed between the U component and the direction of the train's travel. Figure 3 illustrates the boundary conditions, which include velocity inlets and pressure outlets surrounding the computational domain. The ground and tracks are designed as no-slip moving walls, whereas the upper surface utilizes a symmetry boundary. In Scenario B, the windbreak wall has a height of 4 meters, the gap between the walls measures 5 meters, and the nearest distance from the windbreak wall to the track is 5.7 meters. The parameters were selected based on the settings of the Lanzhou-Xinjiang high-speed railway line, as referenced by Liu et al. (2022). The dimensions of the computational domain are identical to those in Scenario A; however, a moving train model is employed, with the train advancing along the positive x-axis at speed V_{train}. The boundary conditions at the interface are established to enable the exchange of flow field data between the moving and static regions. Simultaneously, the ground, track, and windbreak walls are specified to have no-slip conditions.

3.2 Method and Grid Generation

In this study, a stationary train model is employed to simulate the aerodynamic characteristics of the train under crosswinds in Scenario A, while dynamic grid technology is implemented to facilitate train motion in Scenario B. At a train speed of 600 km/h, it is essential to account for air compressibility. Baker (2014) and Zhou et al. (2021) indicate that our objective is to acquire the unsteady aerodynamic loads of the train, taking into account the computational resources. Guo et al. (2023) utilized unsteady Reynolds-averaged Navier-Stokes (URANS) equations alongside the Shear Stress Transfer (SST) k-ω turbulence model, recognized for its efficacy in vehicle aerodynamics and its capability to manage strong separated flows. Li et al. (2019), Zhang (2016) are utilized to model the unsteady aerodynamic behavior of a three-car maglev train operating at a speed of 600 km/h. The URANS model is not designed to capture the high frequencies linked to the smallest turbulent eddies. Rather, it emphasizes the broader unsteadiness that can substantially affect the dynamics of the train. In this study, STAR-CCM+ is utilized to create a trimmed cell mesh for partitioning the flow field, along with a prism layer mesh adjacent to the train surface to accurately capture the flow in the boundary layer. Solving the flow within the viscous sublayer requires a sufficiently refined mesh near the wall, with a $y+$ value close to 1 or lower for the near-wall grids. The initial grid point must be positioned within the viscous sublayer to guarantee that the $y+$ values across the majority of the train surface remain below 1. This study establishes 23 layers of prismatic grids with a growth rate of 1.2, yielding a total thickness of 3.26 mm. This study utilizes a second-order upwind scheme for discretizing the diffusion and turbulence terms. The time advancement utilizes an implicit second-order accurate scheme, employing a time step of 0.4 ms to maintain a Courant-Friedrichs-Lewy (CFL) number below 1.

$$\mathrm{CFL} = V \cdot \Delta t / \Delta x \tag{1}$$

Here, V represents the free-stream velocity, Δt is the time step size, and Δx is the grid size dimension.

In Scenario A, the study refines the mesh near the maglev train, referencing crosswind studies conducted by Chen et al. (2019), as shown in Fig. 4. The minimum grid L_{min} dimension near the vehicle and tracks is 50 mm. Three

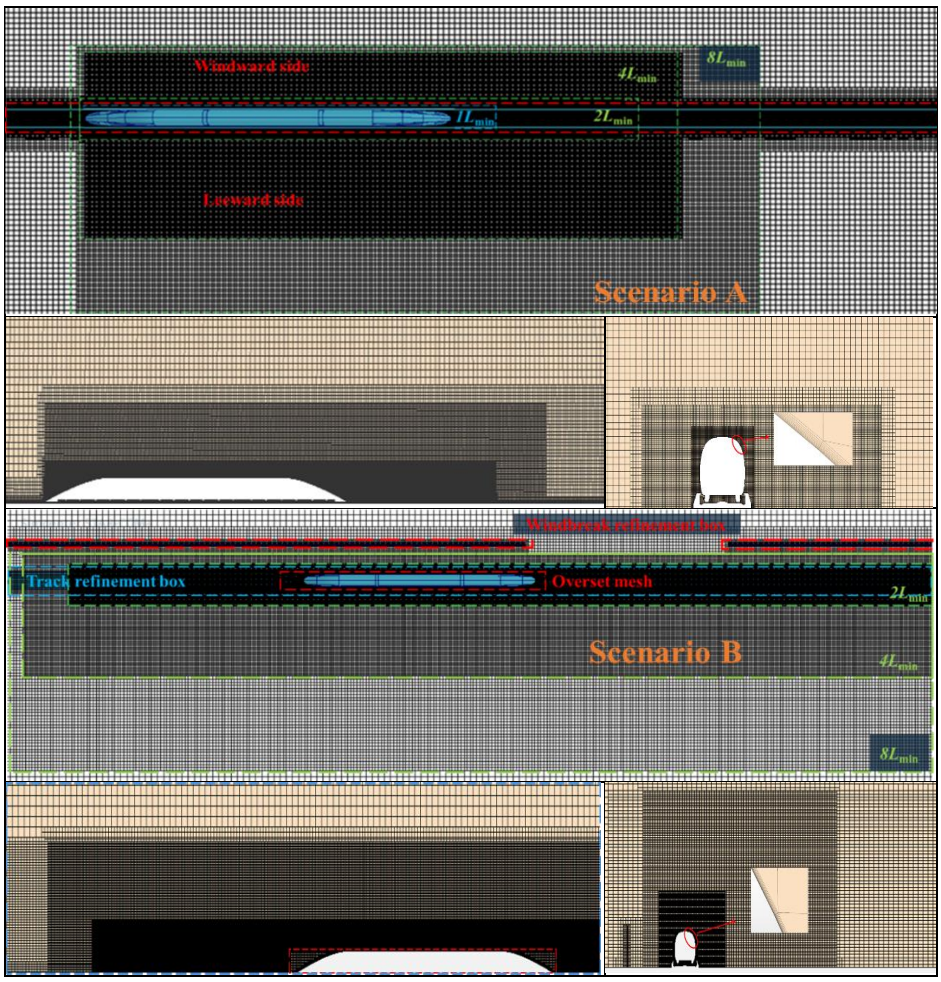

Fig. 4 Grid generation distribution for Scenario A and B

refinement blocks surrounding the train increase this dimension to 8 times the original size, yielding approximately 31.8 million cells. In Scenario B, the minimum mesh near the train and track is L_{min} (50 mm). Additionally, three zones for mesh refinement have been established. The initial zone concentrates on the underbody and the adjacent wake region. The second zone enhances the mesh resolution around the windbreak and the HTS maglev train. The third computational domain zone improves mesh resolution in the vicinity of the windbreak, track, and train, culminating in a total of 35.4 million cells. Three grid configurations (coarse, medium, and fine) are generated for Scenario A to verify the mesh independence of the simulation results. Table 1 summarizes the minimum grid size and the corresponding cell counts for these grids. The monitoring lines on the maglev train's upper surface extend from the nose of the head car at coordinates (0,0,0) to the nose of the tail car at (0, 61.36 m, 0) for the purpose of observing the pressure coefficient C_p. Following numerical calculations with three grid densities, the section details the drag coefficient C_d and C_p along the monitoring line, defined as:

$$C_d = \frac{2F_d}{\rho A_{train} U^2} \tag{2}$$

$$C_p = \frac{2(P - P_\infty)}{\rho U^2} \tag{3}$$

Where F_d is the aerodynamic drag; ρ is the air density,1.225 kg/m^3; A_{train} is the orthographic area of the maglev train, 8.47 m^2 here; U is the resultant velocity; P and P_∞ are the surface static pressure of the train, the reference pressure in the far-field (101325 Pa), respectively. Table 1 presents the drag coefficient C_d of the maglev train for three grid densities, revealing that the medium grid's C_d closely matches the fine grid's, with an error of about 0.47%, which is approximately one-fifth of the coarse grid's error relative to the fine grid. Figure 5 displays the pressure coefficient C_P distribution on the top surface of the maglev train for these grids, indicating a consistent trend. The medium grid's C_P distribution is more similar to the fine grid, especially at the train's ends. Hence, grid density has minimal impact on the train's drag and pressure when the cell count is over 31 million.

Table 1 Three different density grid Settings and drag coefficient of the maglev train

	Coarse	Medium	Fine
L_{min}	0.065 m	0.05 m	0.035 m
Number of cells / million	25.09	31.82	42.64
C_d	0.269	0.263	0.261
Error with fine Gird's C_d	2.61%	0.47%	—

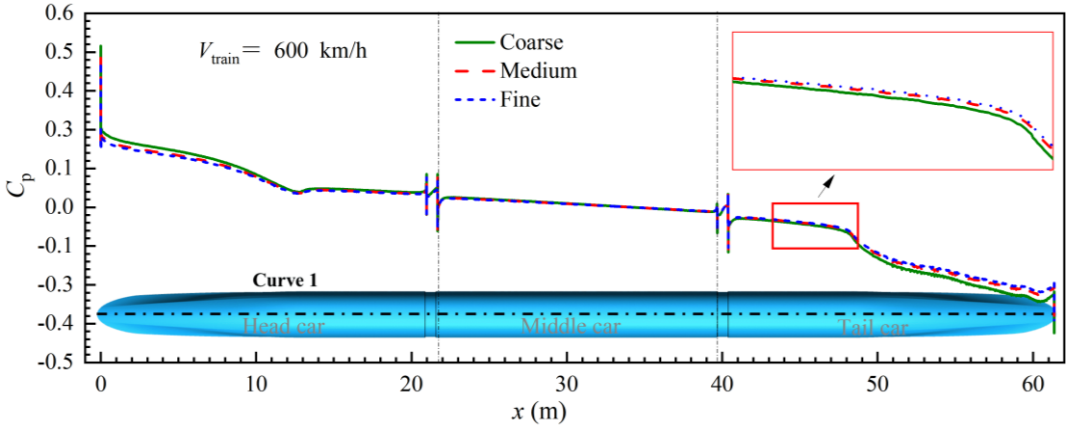

Fig. 5 Pressure coefficient C_p distribution along the top of the maglev train, as calculated with three grid densities

Table 2 ICE2 1:10 scaled model wind tunnel experiment setting

Experimental parameter	Value
Resultant wind velocity (U)	70 m/s
Wind angle (β)	30°
Turbulence intensity (I)	0.5%
Reynolds number (Re)	1.4×10^6

3.3 Numerical Validation

Currently, there is an absence of wind tunnel or full-scale experimental data for HTS high-speed maglev prototypes. This research utilizes a 1:10 scaled model of the German ICE-2 train for simulation calculations in crosswind conditions, comparing the results with experimental data obtained from wind tunnel tests. The experimental parameters for comparison in the ICE-2 wind tunnel are presented in Table 2. Figure 6 (a) presents the 1:10 scale model of the ICE-2 train, which comprises a head car and a tail car. The model's dimensions align closely with those of the wind tunnel test model presented in the literature by Hemida and Krajnovic (2009), though it lacks specific features such as bogies, obstacle removers, and roof air conditioning units. The height H_I of the train model is approximately 0.41 m, the width is about 0.74 H_I (0.302 m), and the total length is L_I (3.58 m. The front car measures approximately 6.59 H_I (2.69 m) long and the tail car about 2.18 H_I (0.89 m) long. The numerical validation computational domain configuration for the ICE-2 aligns with that of the HTS maglev train model in this study, as illustrated in Fig.6 (b). Boundaries replicate the characteristics of a wind tunnel, featuring free-stream inlets and outlets, a symmetrical top, and no-slip walls for both the train and the ground. The meshing and solving settings closely resemble those of scenario A.

Figures 6 (c) and (d) present a comparison of computational results with wind tunnel test data for the ICE2 model, while Fig. 6 (a) delineates the two car body cross-sections utilized for this comparison. The simulation aligns closely with the experimental data, with the exception of the underside ($135° < \theta < 225°$), where the experimental model incorporates an undercarriage absent in this study's model. This leads to a greater discrepancy, though it remains within an acceptable error margin. The results confirm the accuracy and suitability of the employed numerical methods.

3.4 The Definition of Aerodynamic Loads

This study simulates an incoming flow velocity of 600 km/h, resulting in a Reynolds number in the order of 10^6, indicating that inertia dominates the air movement, while the effect of air viscosity is mainly observed within the boundary layer. This study analyzes the distribution and characteristics of aerodynamic loads on trains in both time and frequency domains. This study defines and elucidates the various types of aerodynamic loads.

$$F_x = F_{px} + F_{\tau x} = \iint_s (p_x + \tau_x) \tag{4}$$

$$F_y = F_{py} + F_{\tau y} = \iint_s (p_y + \tau_y) \tag{5}$$

$$F_z = F_{pz} + F_{\tau z} = \iint_s (p_z + \tau_z) \tag{6}$$

The aerodynamic forces on a car and bogie, represented as F_x, F_y, and F_z for drag force, lateral force, and lift force respectively, are determined using the formulas outlined in equations (4), (5), and (6). The overall force in each direction is the vector sum of the pressure and shear stress components present in that direction. F_{pi}, where i=x, y, z, denotes the pressure difference forces along the x, y, and z axes, respectively. Similarly, $F_{\tau i}$, with i=x, y, z, represents the shear forces in the x, y, and z axes, respectively. The variables p_i and τ_i correspond to pressure stress and shear stress along the x, y, and z axes, respectively. The overturning, pitching, and rolling characteristics of the high-speed maglev train, alongside the aerodynamic forces in three directions, merit careful consideration. To ascertain the moment, it is essential to first identify the center and axis of the moment. The moment center presented in this paper is derived as illustrated in Fig. 7. The overturning moment results from the lift force and lateral force, calculated by summing the moments about the longitudinal axis that intersects the lower surface of the leeward side suspension bogie for each point on the train. The overturning moments for the

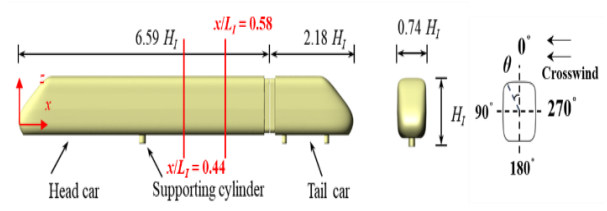

(a) ICE-2 geometry model and the definition of section position and angle θ

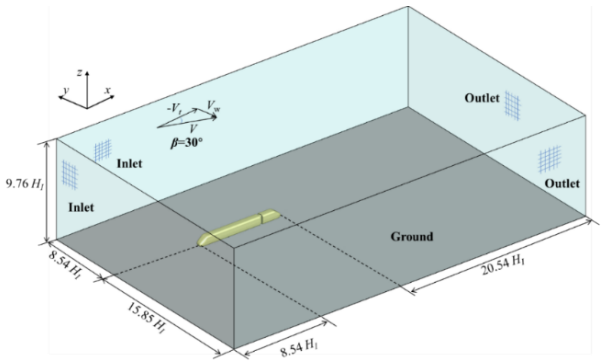

(b) The computational domain of the ICE-2

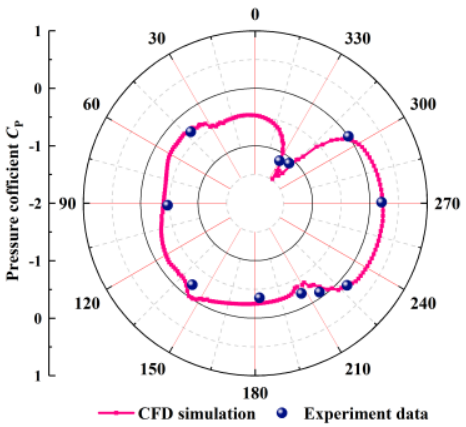

(c) x/L_I =0.44 pressure coefficient

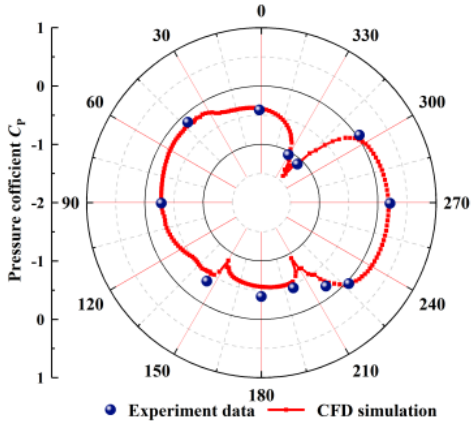

(d) x/L_I =0.58 pressure coefficient

Fig. 6 Schematic diagram of the computational domain setup and mesh division for the validation case (a)-(b). Comparison of wind tunnel experimental data with the simulation results of ICE-2 body surface pressure coefficient (c)-(d)

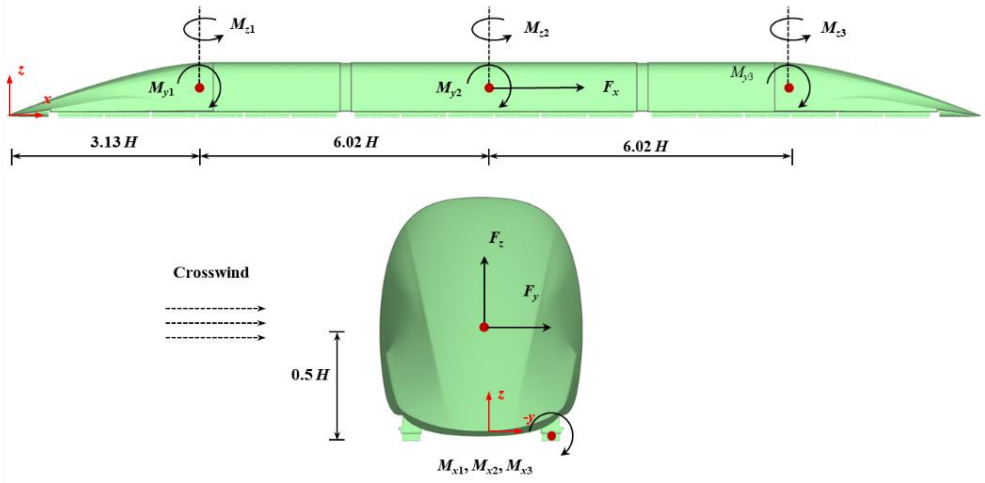

Fig.7 The position of the aerodynamic moments center

head, middle, and tail cars are represented as M_{x1}, M_{x2}, *and* M_{x3}, respectively. The pitching and yawing moments are obtained at the center of each of the three vehicles. The pitching moments for the head, middle, and tail cars are denoted as M_{y1}, M_{y2}, and M_{y3}, while the yawing moments are represented as M_{z1}, M_{z2}, and M_{z3}, respectively.

3.5 HTS Maglev Train MBD Model

This section outlines the vehicle dynamics model derived from the HTS maglev head vehicle prototype, as illustrated in the topology diagram in Fig. 8. The research includes the main rigid bodies and force components in the model. The car body and suspension bogies represent the

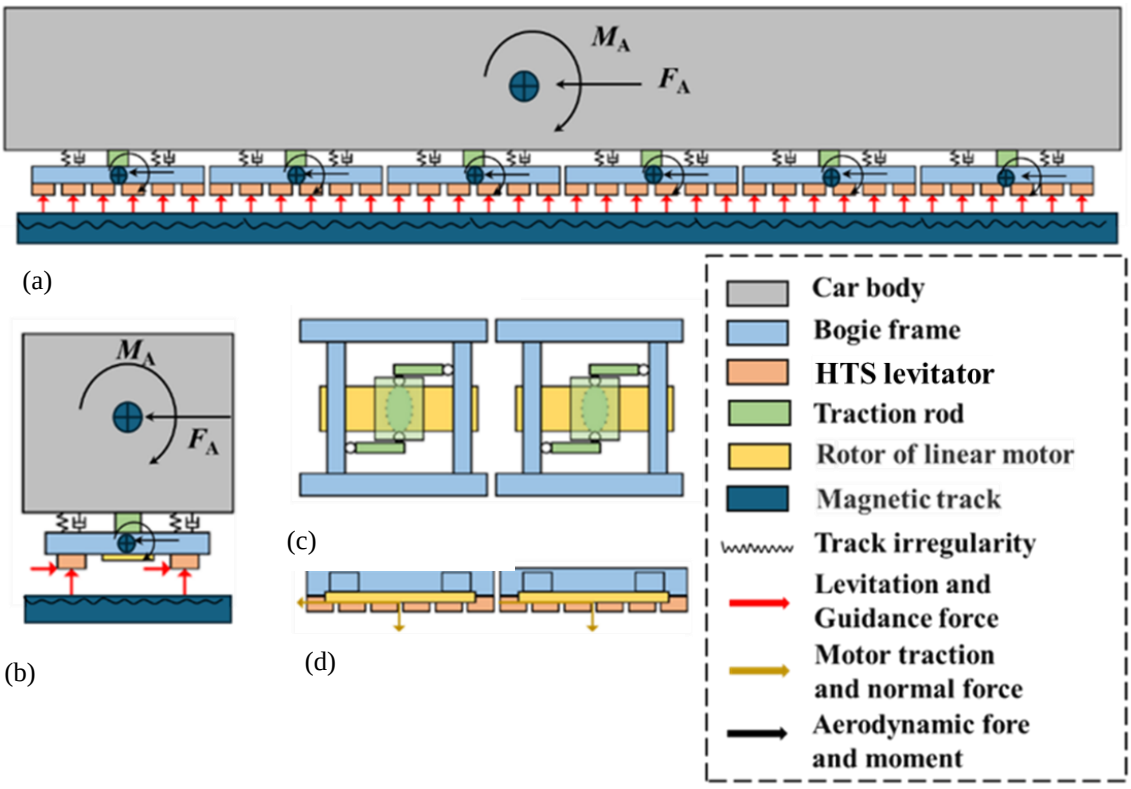

Fig. 8 Dynamic topology diagram of a single vehicle

primary rigid structures in motion, with the HTS levitator affixed to the suspension frame. This configuration is essential for evaluating the dynamic responses in crosswind scenarios. The Z-shaped traction rod transmits traction force independent of its mass, as demonstrated in Fig. 8 (c) and (d). The train consists of three cars, nine suspension bogies, and 216 HTS levitators, each equipped with levitation and guidance force elements at the base. The interaction between the PMG and the superconducting bulk material of the levitator, referred to as the magnetic-track relationship, mathematically characterizes the forces of levitation and guidance. The research cites Kou et al. (2021) regarding the magnetic rail relationship and employs irregularity data from the Shanghai Maglev to analyze the magnetic track's irregularity. The comprehensive train dynamics model comprises 12 rigid bodies, each possessing 6 degrees of freedom, resulting in a total of 72 degrees of freedom. The parameters of the single-vehicle model are presented in Table 3 (Hu et al., 2024). In the context of HTS maglev trains, "car" refers to the carriage, while "vehicle" encompasses both the car body and the underlying suspension bogies.

Table 3 Parameters of HTS maglev vehicle (single vehicle)

	Terms	Value	Units
m_c	Car body mass	2.3×10^4	kg
I_{cx}	Car body rolling inertia	5.6×10^4	kg/m^2
I_{cy}	Car body pitching inertia	1.50×10^6	kg/m^2
I_{cz}	Car body yawing inertia	1.51×10^6	kg/m^2
m_f	Bogie mass	1.681×10^3	kg
I_{fx}	Bogie rolling inertia	6.8×10^3	kg/m^2
I_{fy}	Bogie pitching inertia	9.7×10^3	kg/m^2
I_{fz}	Bogie yawing inertia	2.3×10^4	kg/m^2
K_{sy}	Air spring lateral stiffness	3.25×10^4	N/m
K_{sz}	Air spring vertical stiffness	5×10^4	N/m
C_{sy}	Air spring lateral damping	5×10^3	N·s/m
C_{sz}	Air spring vertical damping	5×10^3	N·s/m

4. RESULTS AND DISCUSSION

4.1 Aerodynamic Characteristics and Loads of Scenario A

This section initiates a detailed analysis of the aerodynamic load characteristics of the HTS maglev pinning train in Scenario A. Figure 9 (a) illustrates the pressure contour on the train's surface and the pressure distribution curves along the body cross-section at z = 1.2 m. The curves indicate that in both the head car and middle car sections, the pressure on the windward side exceeds that on the leeward side, exhibiting positive pressure distribution on the windward side and negative on the leeward side. The pressure distribution at the streamlined tail car contrasts with that of the initial two sections, exhibiting negative pressure on the windward side and positive pressure on the leeward side. The negative pressure

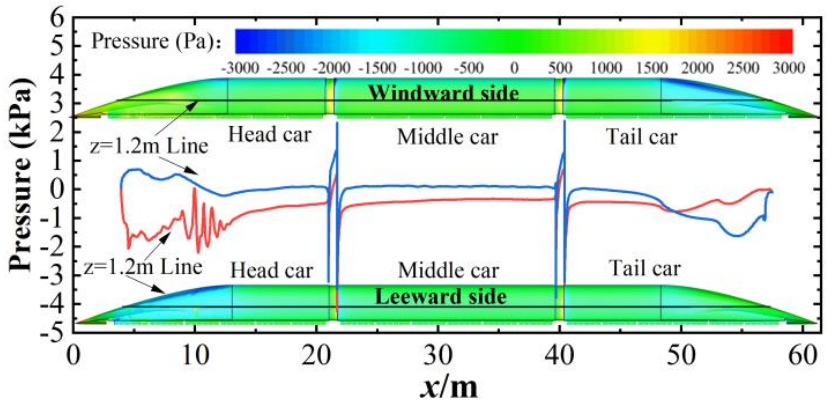

(a) Pressure distribution along the z=1.2 m section and the surface pressure contour of the train body

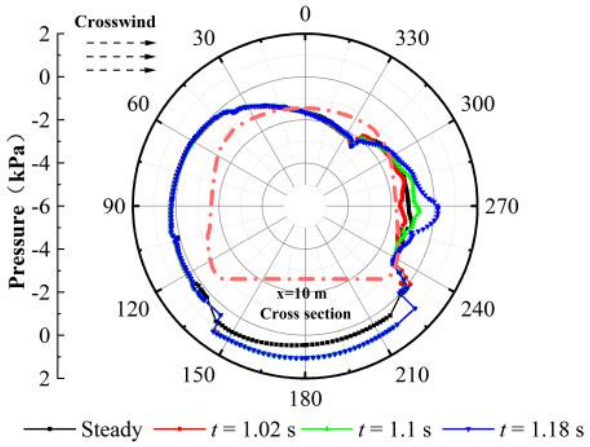

(b) Pressure distribution in x=10 m

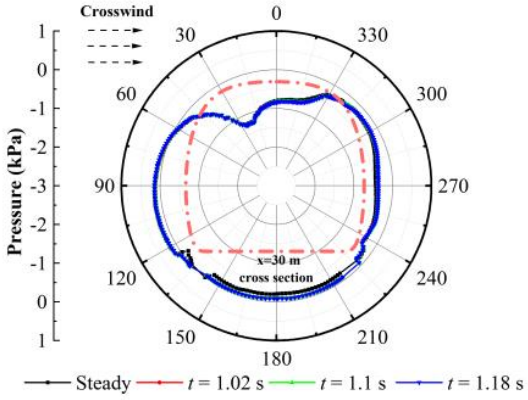

(c) Pressure distribution in x=30 m

Fig. 9 Cross-sectional surface pressure distribution and the surface pressure contour of the train body

on the windward side of the tail car results from the separation of airflow over the streamlined surface. The positive pressure observed on the leeward side arises from the interaction of crosswinds with the train's wake, which is deflected towards the leeward side. This wake is impeded by the semi-enclosed track of the HTS maglev, leading to the formation of a high-pressure area adjacent to the tail car and the track on the leeward side. The interaction of these two factors produces a pressure distribution on the tail car surface that contrasts with that of the initial two sections. The analysis of aerodynamic loads indicates that the lateral force on the tail car acts in the opposite direction to that on the first two cars, a phenomenon resulting from the differing surface pressure distributions across the vehicle bodies. The sectional variation of the windshield causes flow stagnation and separation, leading to significant pressure fluctuations, decreasing from 2.1 kPa to -4.5 kPa at the windshield locations. Figures 9(b) and (c) present a comparison of transient surface pressures at three time points, t=1.02, 1.1,

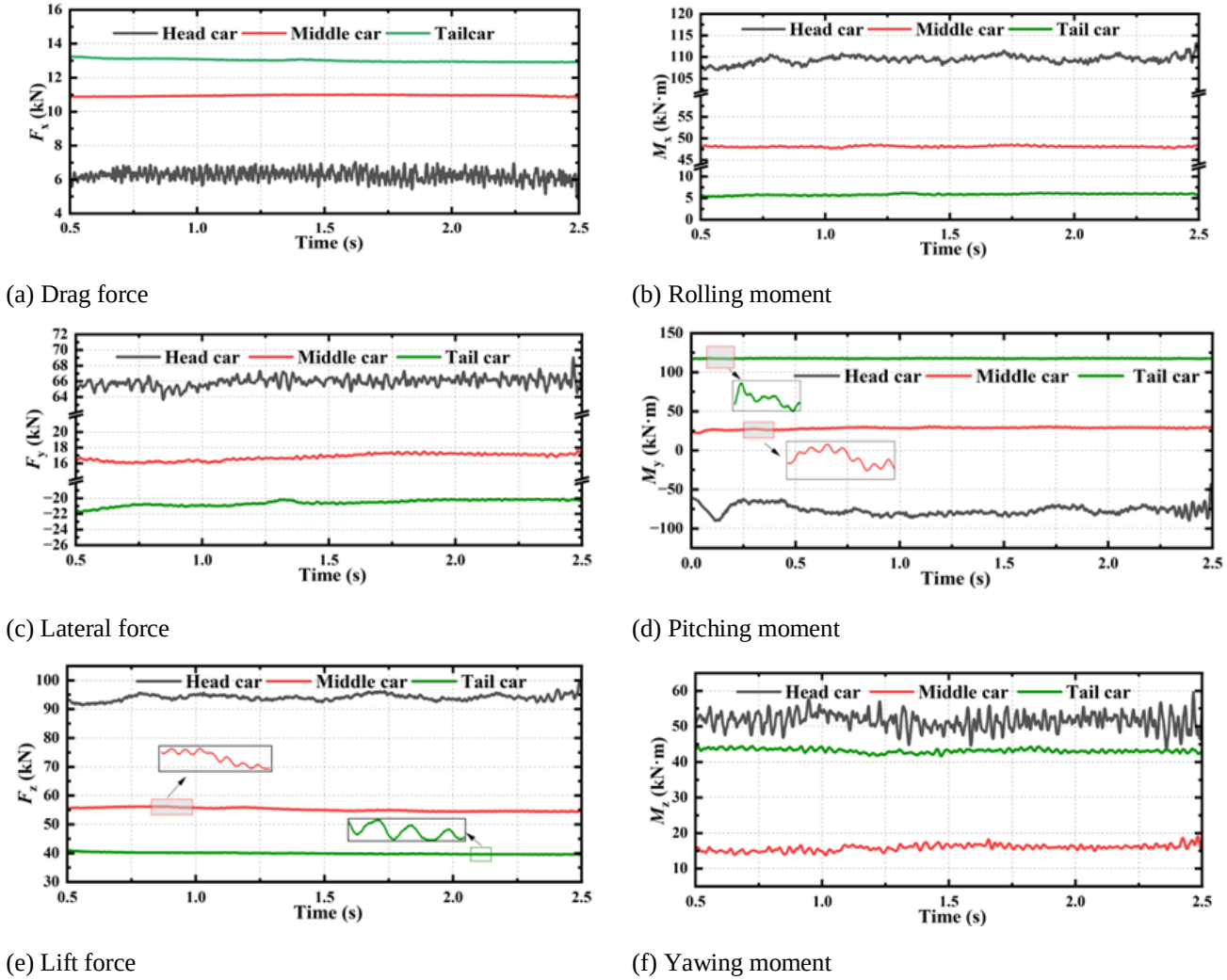

(a) Drag force

(b) Rolling moment

(c) Lateral force

(d) Pitching moment

(e) Lift force

(f) Yawing moment

Fig. 10 Aerodynamic loads of the car body

and 1.18 seconds, against steady-state calculations. The pressures are shown for the head car at x=10 m in (b) and for the middle car at x=30 m in (c). At x=30 m, the pressure distribution remains consistent over time and correlates closely with steady-state results. At x=10 m, the windward side of the vehicle surface shows minimal pressure fluctuations, with pressures at various times aligning closely with the steady-state results, whereas the leeward side displays significant variations. The unsteady load characteristics of a train are influenced by the local structure of the car body. Smoother surfaces and gradual geometric transitions lead to milder unsteady traits and uniform flow, while sharp geometric changes result in significant flow separation and pressure pulsations.

Simulations involve monitoring the train's critical aerodynamic loads to obtain time history curves, facilitating an analysis of their time-domain unsteadiness. Power spectral density (PSD) calculations are conducted to assess the energy contributions of frequency components to the loads. This section employs specific values of force and moment to directly illustrate the magnitude and fluctuation patterns of aerodynamic loads, thereby aiding their integration into the dynamics model of the HTS superconducting maglev train. Figure 10 illustrates the temporal variations of aerodynamic loads acting on the maglev train. The analysis is restricted to data from 0.5 to 2.5 seconds to mitigate errors arising from the non-convergence of initial transient calculations. The data indicate that all vehicles experience unsteady aerodynamic loads, with the head car exhibiting the most pronounced fluctuations. The tail car exhibits the highest average aerodynamic drag, followed by the middle car, while the head car demonstrates the lowest drag. Nonetheless, the head car demonstrates the highest amplitude, amplitude ratio, and standard deviation of drag, suggesting that despite a lower average drag, it undergoes the most significant fluctuations. The pressure drag component for the head car section is negative, whereas the viscous drag is comparatively significant, leading to an overall aerodynamic drag that is lower than that of other car bodies. The middle and tail cars exhibit reduced variation in loads such as drag and lift, with minimal high-frequency oscillations in comparison to the head car. Tables 4 and 5 display the aerodynamic loads on the train, detailing the mean, maximum amplitude, and standard deviation. The tail car exhibits the highest mean drag, whereas the head car shows the lowest mean drag but undergoes the most intense pulsations. The head car registers the highest values for lateral force, while the tail car demonstrates a negative force opposing the direction of the crosswind. The head car exhibits a notably higher mean lift than both the middle and tail cars, accompanied by the most substantial fluctuations. The head car exhibits

Table 4 Aerodynamic forces of the car body

Car	Drag (kN)			Lateral force (kN)			Lift (kN)		
	Mean value	Maximum amplitude	Standard deviation	Mean value	Maximum amplitude	Standard deviation	Mean value	Maximum amplitude	Standard deviation
Head car	6.16	1.43	0.21	66.95	3.58	0.41	92.70	5.60	0.71
Middle car	9.30	0.12	0.03	17.19	1.08	0.28	56.79	1.23	0.40
Tail car	10.67	0.22	0.06	-22.72	1.13	0.25	40.62	1.01	0.21

Table 5 Aerodynamic moments of the car body

Car	Roll moment (kN·m)			Yaw moment (kN·m)			Pitch moment (kN·m)		
	Mean value	Maximum amplitude	Standard deviation	Mean value	Maximum amplitude	Standard deviation	Mean value	Maximum amplitude	Standard deviation
Head car	109.44	6.25	0.88	51.57	15.89	2.27	-74.41	44.91	8.31
Middle car	48.11	0.92	0.17	15.89	5.30	0.82	32.37	15.99	3.46
Tail car	5.58	0.84	0.18	43.20	2.78	0.54	120.24	9.97	1.64

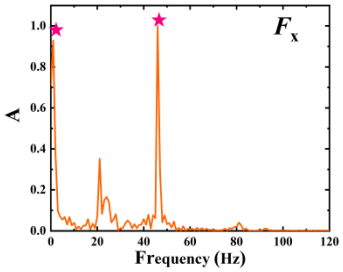

(a1) Head car drag Power spectral density

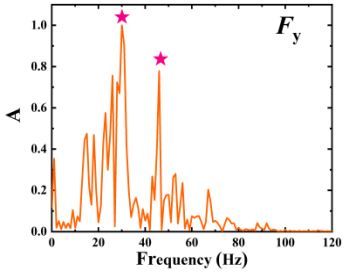

(a2) Head car lateral force Power spectral density

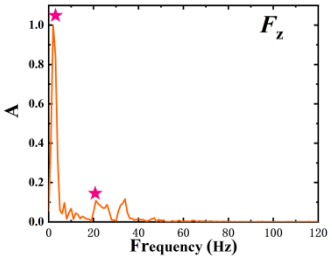

(a3) Head car lift force Power spectral density

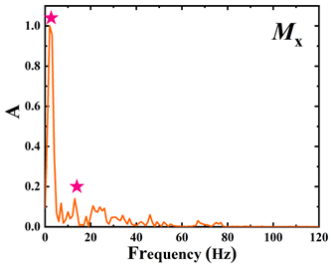

(a4) Head car M_x Power spectral density

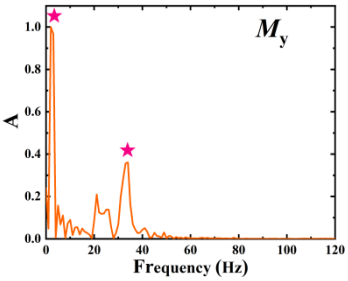

(a5) Head car M_y Power spectral density

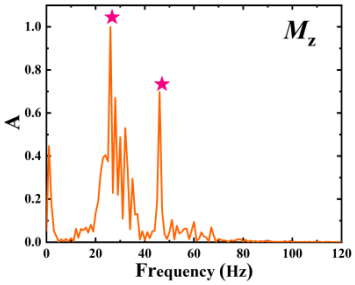

(a6) Head car M_z Power spectral density

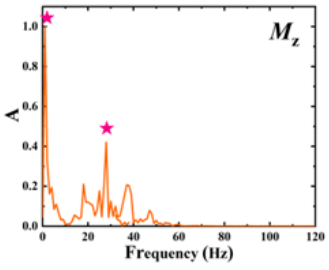

(b1) Middle car M_z Power spectral density

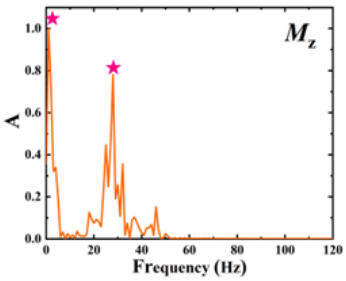

(b2) Tail car *Mz* Power spectral density

Fig. 11 Power spectral density distribution of the aerodynamic loads

the highest rolling and yawing moments, whereas the tail car displays the lowest values. The pitching moment of the tail car exhibits the highest absolute value, while the negative value of the head car indicates a tendency that may compromise safety by lifting and raising the tail. The lead vehicle faces significant aerodynamic challenges and safety concerns in crosswind conditions.

Figure 11 (a1) - (a6) presents the Power Spectral Density (PSD) distribution of the aerodynamic loads across various train car body configurations. At a speed of V_{train}=600 km/h, the peak frequencies of the aerodynamic load PSD for each carriage are predominantly within 60 Hz, categorized into two frequency ranges: low frequencies from 1 to 5 Hz and higher frequencies exceeding

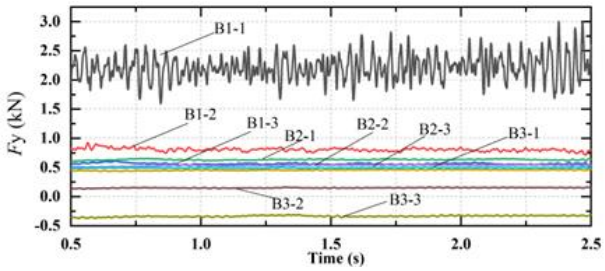

(a) Lateral force-time curve of bodies

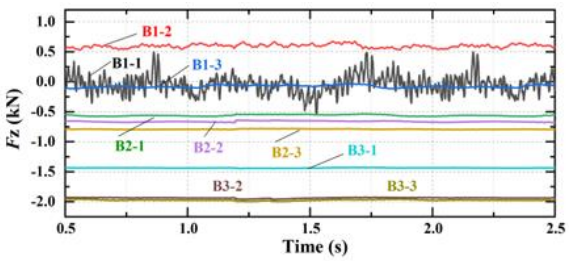

(b) Lift force-time curve of bodies

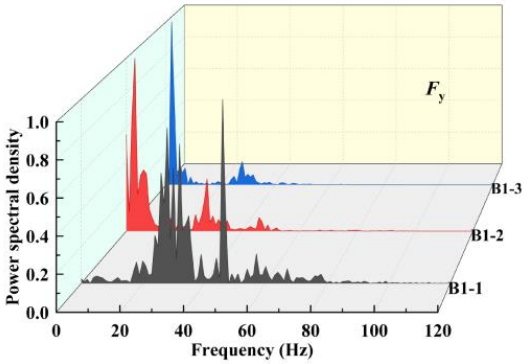

(c) The PSD distribution of the lateral force on the head car's bodies

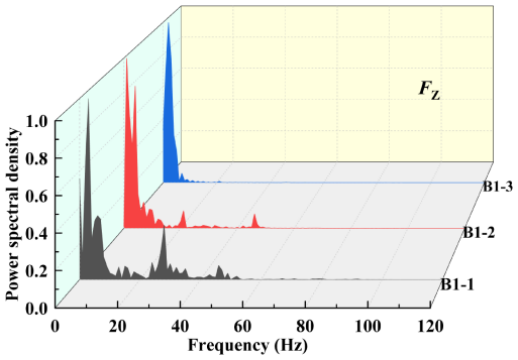

(d) The PSD distribution of the lift force on the head car's bodies

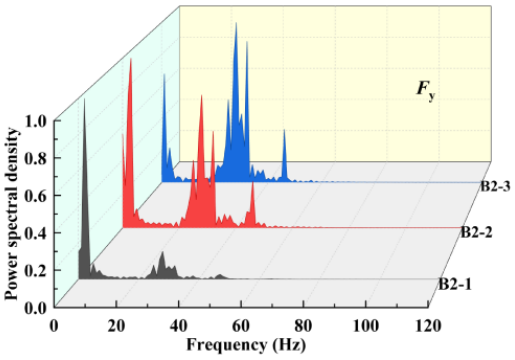

(e) The PSD distribution of the lateral force on the middle car's bodies

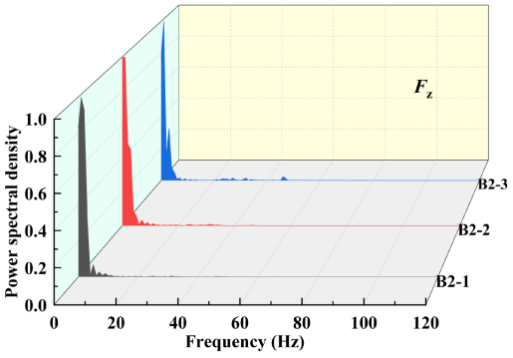

(f) The PSD distribution of the lift force on the middle car's bodies

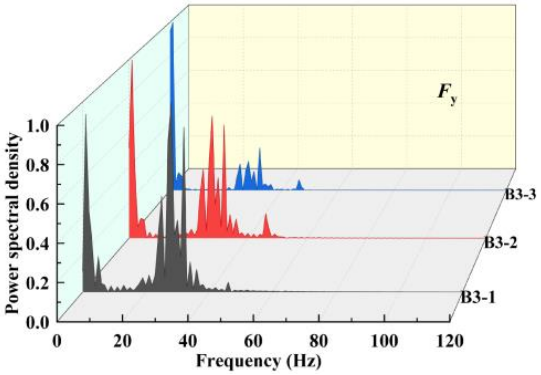

(g) The PSD distribution of the lateral force on the tail car's bodies

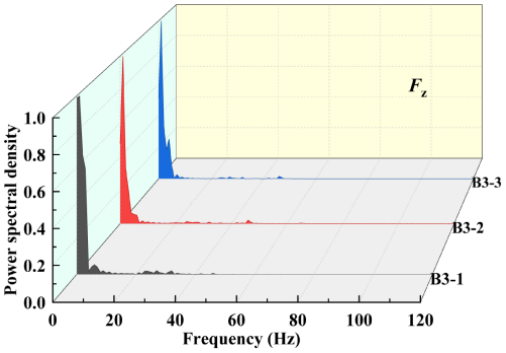

(h) The PSD distribution of the lift force on the tail car's bodies

Fig. 12 Time curve and PSD distribution of bogies

10 Hz. The head car exhibits the broadest peak frequency distribution, with frequencies ranging from 10 to 50 Hz for lateral forces, suggesting a potential for resonance with the car body across a wide frequency spectrum. In the middle and tail cars, aside from the yawing moment, which exhibits a pronounced peak in the high-frequency range (refer to Fig. 11 (b1) and (b2)), the predominant frequencies of other loads fall within the low-frequency range of 1 to 5 Hz.

An analysis of the unsteady aerodynamics of suspension bogies is crucial for maglev trains, as lift and lateral forces play a significant role in levitation and guidance characteristics. This study focuses on the analysis of loads on the suspension bogies. Figure 12 (a) and (b) present the time curves for lateral and lift forces across nine bogies, and Fig. 12 (c)-(h) depicting the PSD for each car's bogies. The B1-1 bogie of the head car exhibits the highest lateral force pulsation, reaching a peak

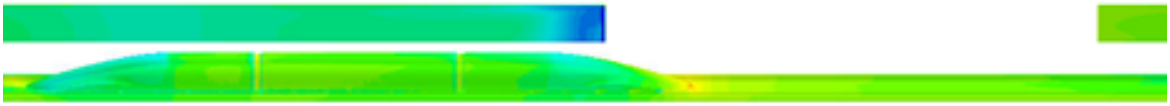

(a) Surface pressure contour of the train body in time=0 s

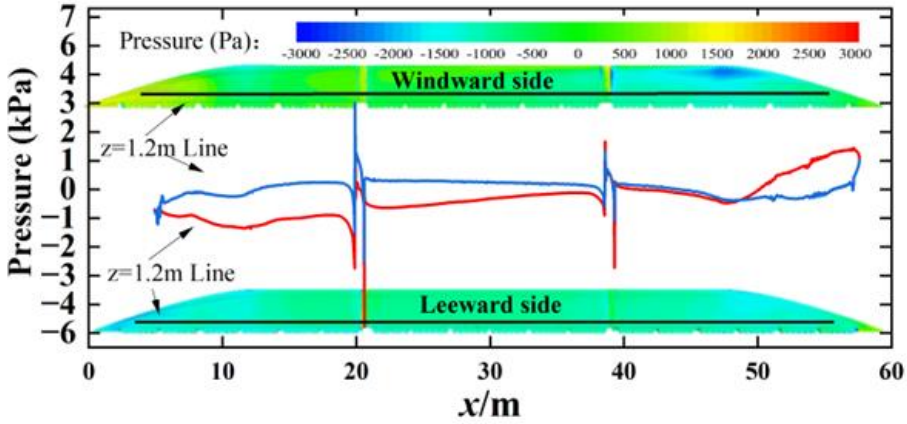

(b) The pressure distribution along the z=1.2 m section

Fig. 13 The pressure distribution along the z=1.2 m section and the surface pressure contour of the train body

of 2.7 kN, with B2-2 following closely behind. The middle and tail car bogies exhibit minimal pulsation, measured at under 0.5 kN, suggesting reduced safety risks. The primary natural frequency of B1-1 is 46 Hz, accompanied by a secondary frequency of 28 Hz, which corresponds to the main aerodynamic load frequency of the head car. Additional bogie frequencies exhibit peaks in two distinct bands: a low-frequency band below 5 Hz and a high-frequency band ranging from 20 to 40 Hz, with a notable peak at 28 Hz, indicative of flow pulsation at this velocity. The fluctuations in lift force for B1-1 are significant, with an amplitude of 1 kN and accompanying directional changes. The B1-2 and B1-3 bogies exhibit positive lift forces, with B1-2 reaching a peak, whereas the others demonstrate downward forces. High-frequency vibrations in the frequency domain are minimized, with only B1-1 and B1-2 displaying vibrations exceeding 20 Hz. To address these effects, measures should be implemented to optimize the bottom flow environment. The lower section of the train, particularly the front B1-1 bogie, may be enclosed, or a flow-guiding device could be implemented at the base of the head car. Furthermore, the U-shaped track of the HTS maglev train partially encases the bogie. Optimization studies can be conducted on critical parameters of the U-shaped track, including the height of the side track.

4.2 Aerodynamic Loads of Scenario B Compared with Scenario A

Figure 13 depicts the initial operational position of the train in Scenario B, including the cross-section at z=1.2 m and the pressure contour on the car body's surface. The pressure curve distribution pattern closely resembles that depicted in Fig.11 of Scenario A. The initial exposure of the head car component to crosswind conditions results in the formation of a high-pressure zone on the windward side of the head car. In the leeward region, the disparity in surface pressure distribution between the leading and trailing vehicles is diminished relative to Scenario A.

Significant aerodynamic load fluctuations are noted in the head car, necessitating a detailed analysis and comparison of its loads with those of its three suspension bogies over the initial 1.4 seconds in Scenario B. The aerodynamic drag curves in Fig. 14 are not presented due to the HTS maglev train dynamics model established in Section 3.5 being a five-degree-of-freedom model that does not incorporate longitudinal loads. Figures 14 (a1) - (e1) illustrate the aerodynamic load time curves for the head car and vehicle, whereas Figures 14(a2) - (e2) present the aerodynamic load curves for the suspension bogies, as the car traverses the windbreak gap from 0 to 0.4 seconds. The presence of the windbreak gap notably increases the range of aerodynamic load fluctuations experienced by both the car body and bogies, reaching a peak within 0.4 seconds and marginally surpassing the loads observed in Scenario A as a result of wind shear. Figure 14 (a2) - (e2) depicts the sequential passage of bogies B1-1, B1-2, and B1-3, with B1-1 exhibiting the most pronounced fluctuations. Prior research consistently applied aerodynamic loads to the entire vehicle. Integrating Fig.14 (a1) - (e1) indicates that the load contribution of the suspension bogies is significant, warranting a partitioned loading analysis in the following study section. Figure 15 illustrates the frequency domain distribution of the head car body and its three bogies in Scenarios A and B, highlighting a significant decrease in high-frequency oscillations in Scenario B. To enhance the comprehension of the influence of the head car's bottom bogies on the aerodynamic load of the car body, Fig. 15 presents a comparison of the frequency domain distribution between the head car body and the bottom bogies across both scenarios. In Scenario B, high-frequency aerodynamic

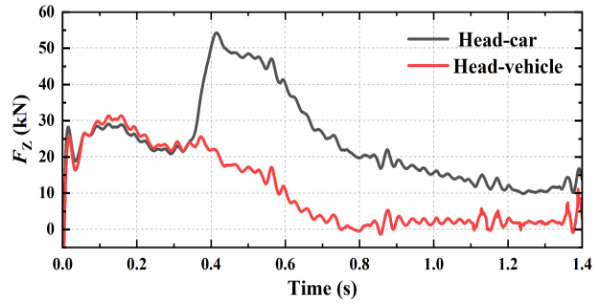

(a1) Lift force of the head car and vehicle

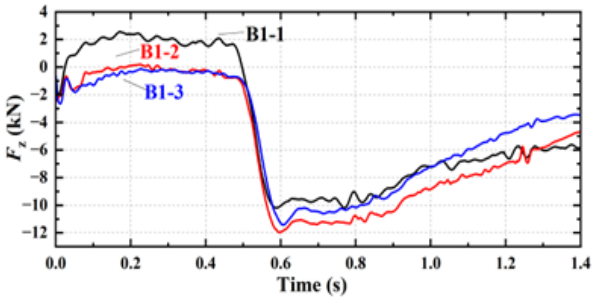

(a2) Lift force of the bogies

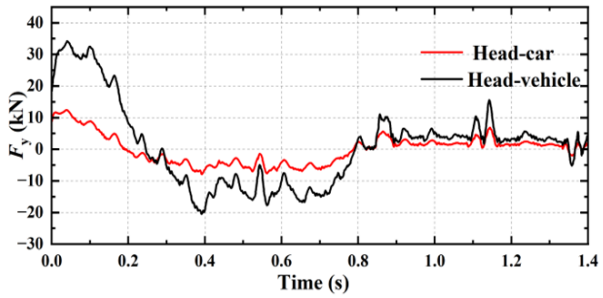

(b1) Lateral force of the head car and vehicle

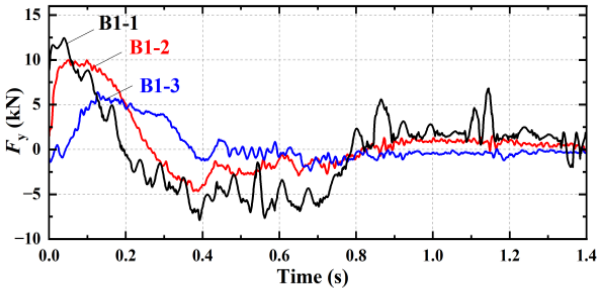

(b2) Lateral force of the bogies

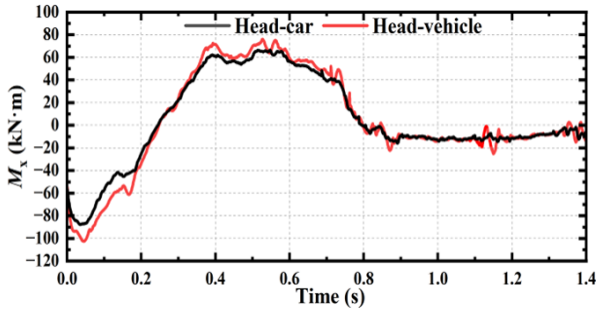

(c1) Rolling moment of the head car and vehicle

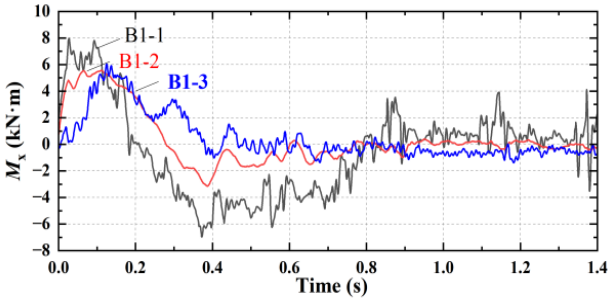

(c2) Rolling moment of the bogies

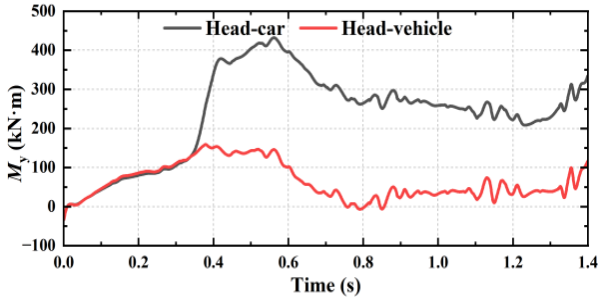

(d1) Pitching moment of the head car and vehicle

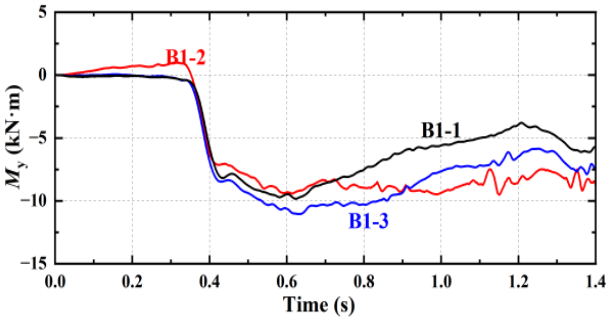

(d2) Pitching moment of the bogies

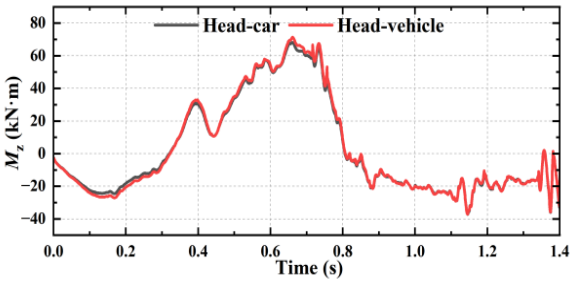

(e1) Yawing moment of the head car and vehicle

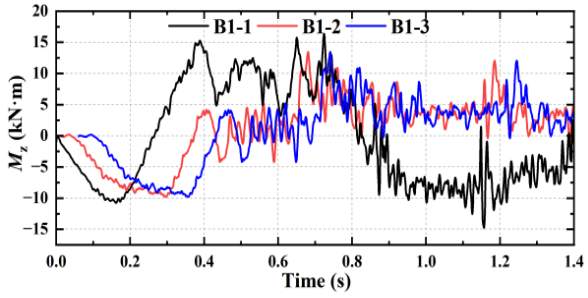

(e2) Yawing moment of the bogies

Fig. 14 Aerodynamic loads time-curve of the head car (car body), head vehicle (car body + bogies), and bogies

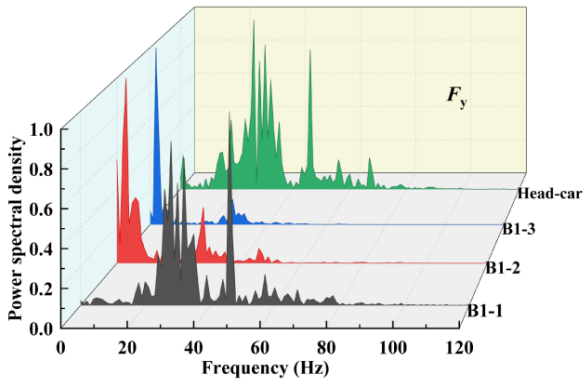

（a1） Lateral force in Scenario A

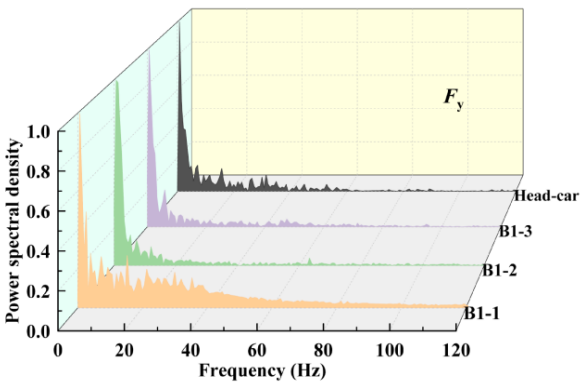

(b1) Lateral force in Scenario B

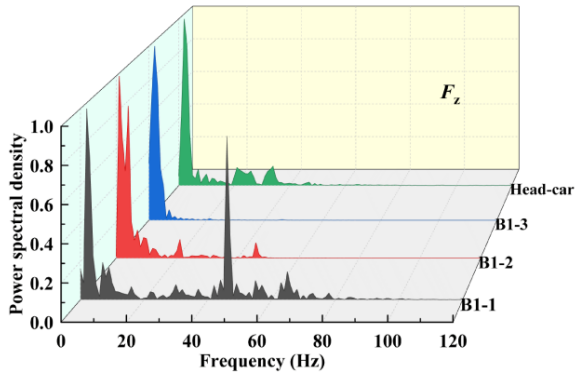

(a2) Lift force in Scenario A

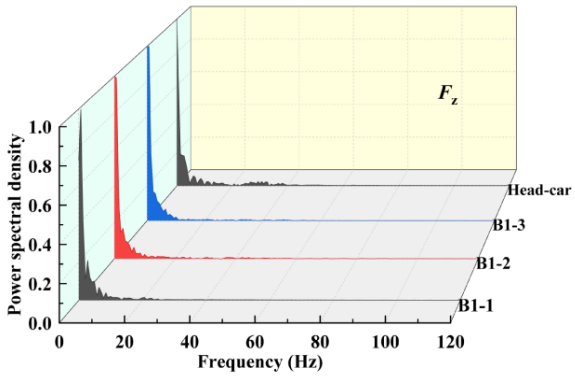

(b2) Lift force in Scenario B

Fig. 15 PSD distribution of the head car and bogies in different Scenarios

load oscillations are significantly reduced. The frequency distribution of the lateral force is more pronounced in the high-frequency range due to crosswind effects, in contrast to the lift force. The comparison reveals that the B1-1 bogie significantly contributes to the high-frequency vibrations affecting the aerodynamic load of the car body.

4.3 Dynamic Response of the HTS Maglev Train

As can be seen from Figures 12(a) and 14(a2) - (e2), in both Scenario A and Scenario B, the bogie of the HTS maglev train encounters considerable aerodynamic lateral forces and lift forces, characterized by notable unsteady fluctuations, particularly in the case of the B1-1 bogie. The overturning moment, pitching moment, and yawing moment constitute the primary aerodynamic loads. The current design of the HTS maglev train features a suspension bogie that is not enclosed by a skirt; instead, it is surrounded by a U-shaped track and is directly exposed to the air, resulting in significant aerodynamic loads.

Following the acquisition of the unsteady aerodynamic loads for the HTS maglev train under crosswinds in Scenarios A and B, these loads are implemented in the multi-body dynamics model outlined in Section 3.4. This study presents the loading method and positions in Fig. 16. Figure 16(a) depicts the locations at which aerodynamic loads are exerted. The loads from the car body and the bogie are applied to their respective centers of mass. To reduce the effects of wind shear on the dynamic response, a 3-second loading phase is implemented prior to and following the application of aerodynamic loads. In Scenario A, the unsteady aerodynamic load fluctuations persist for 2 seconds (from 3 to 5 seconds), as illustrated in Fig. 16 (b). In contrast, Scenario B exhibits fluctuations lasting 1.4 seconds (from 3 to 4.4 seconds), as shown in Fig.16 (c). Additionally, we conducted a comparative analysis utilizing two loading approaches to evaluate the differences in dynamic response when aerodynamic loads are applied separately to the car body and bogie versus when they are applied to the entire vehicle within the vehicle dynamics model. To evaluate the safety of the HTS maglev train's operation in the specified scenarios, the overturning coefficient D is defined in the literature by Wang et al. (2023). The formula is presented below:

$$D = \left| \frac{P_2 - P_1}{P_2 + P_1} \right| \tag{3}$$

P_1 represents the cumulative levitation force exerted on the right side of a vehicle, while P_2 indicates the total levitation force acting on the left side. The safety threshold for the overturning coefficient D is established at 0.8 to mitigate the risk of overturning and associated accidents.

Figure 17 (a1) - (i1) presents the dynamic responses obtained through the partitioned independent loading method, whereas (a2) - (i2) depict the dynamic responses from the whole-vehicle loading method. Additionally, (a1), (b1), and (c1) show the variations in guidance and levitation forces, along with the displacement of levitators for the first row in the B1-1 configuration. The guidance

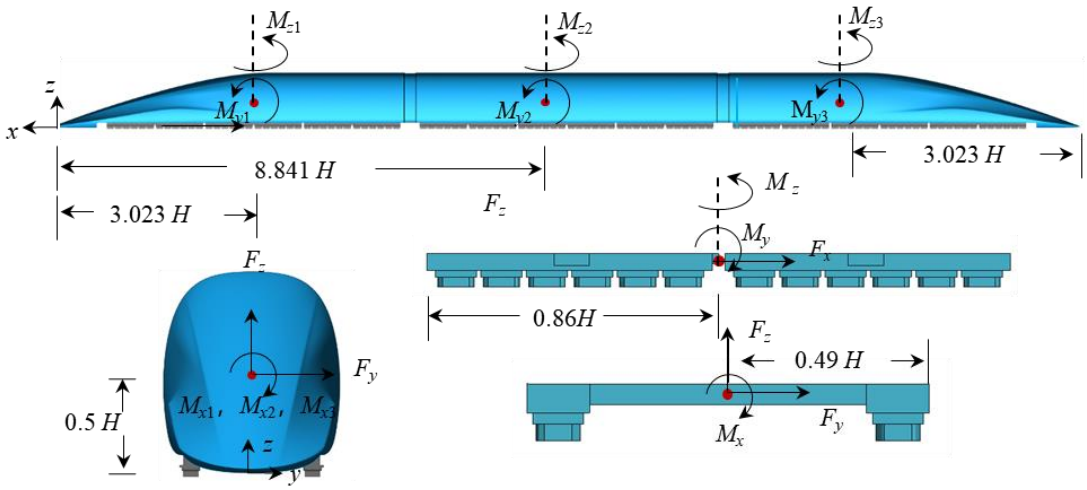

(a) The extraction center of aerodynamic loads

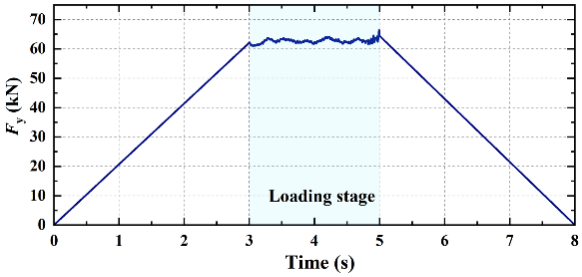

(b) The loading process in Scenario A

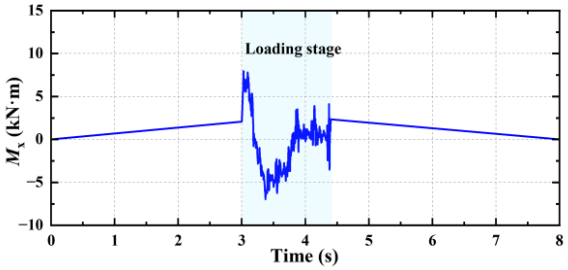

(c) The loading process in Scenario B

Fig. 16 Aerodynamic loads loading method and position of the HTS maglev train

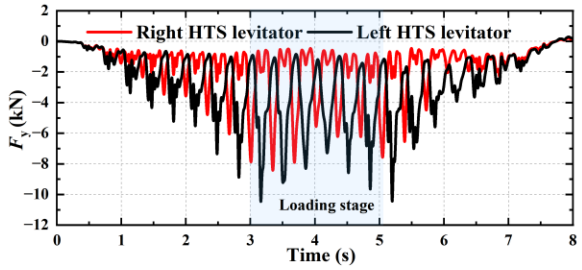

(a1) Guidance force

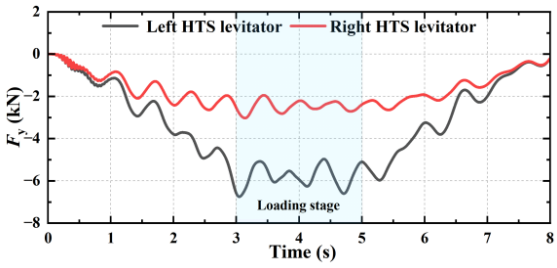

(a2) Guidance force

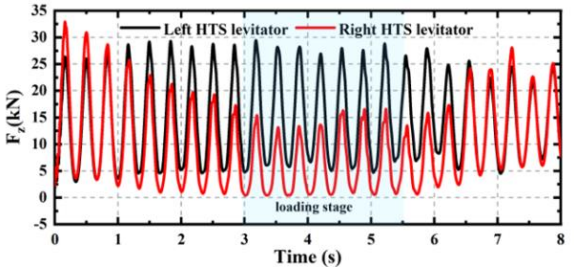

(b1) Levitation force

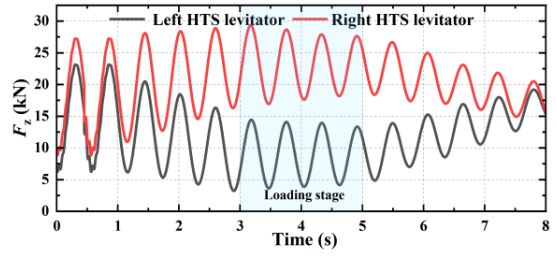

(b2) Levitation force

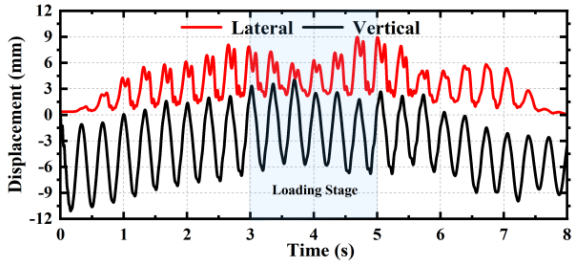

(c1) Vertical and lateral displacement

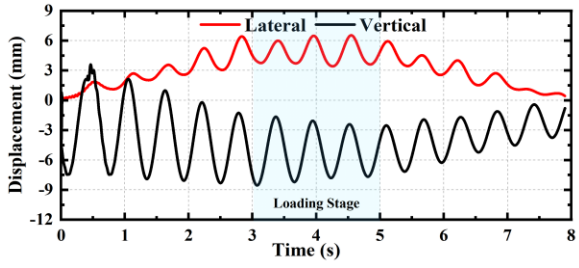

(c2) Vertical and lateral displacement

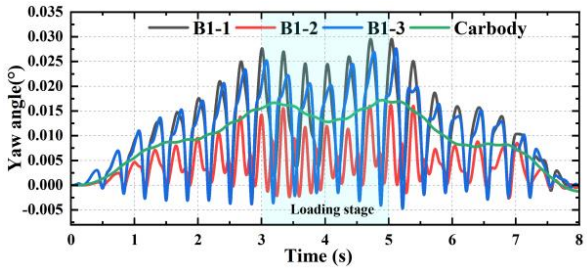

(d1) Yaw angle of the car body and bogies

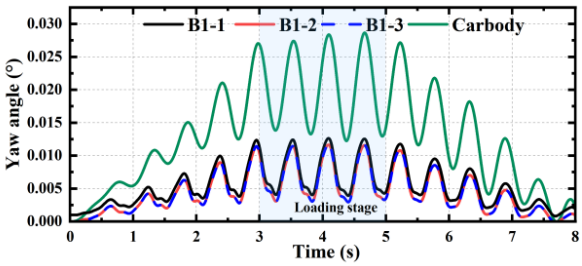

(d2) Yaw angle of the car body and bogies

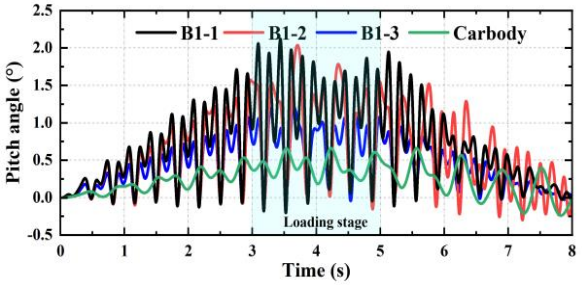

(e1) Pitch angle of the car body and bogies

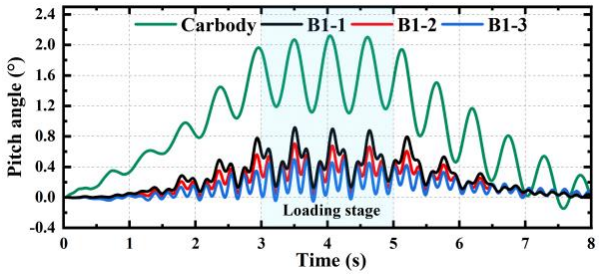

(e2) Pitch angle of the car body and bogies

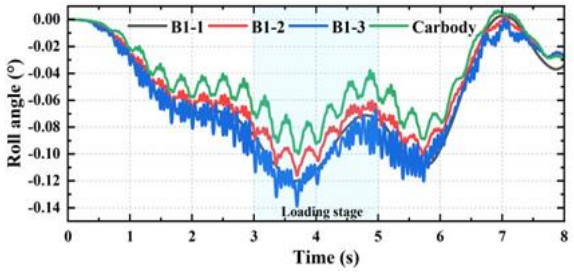

(f1) Roll angle of the car body and bogies

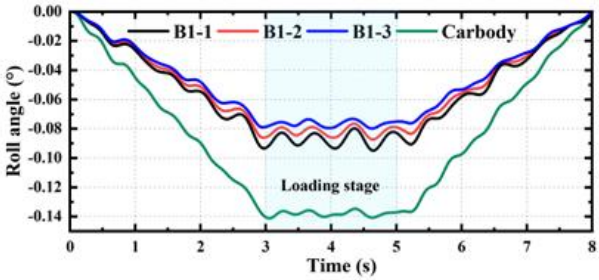

(f2) Roll angle of the car body and bogies

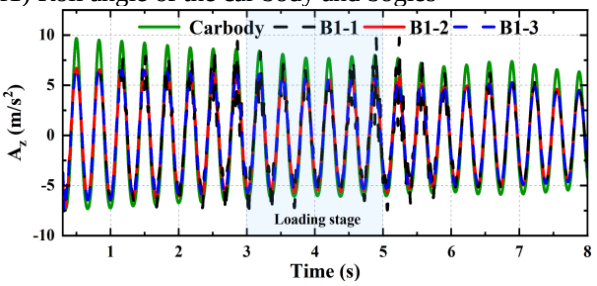

(g1) Vertical acceleration of the car body and bogies

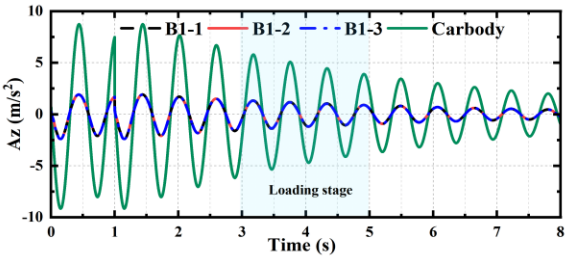

(g2) Vertical acceleration of the car body and bogies

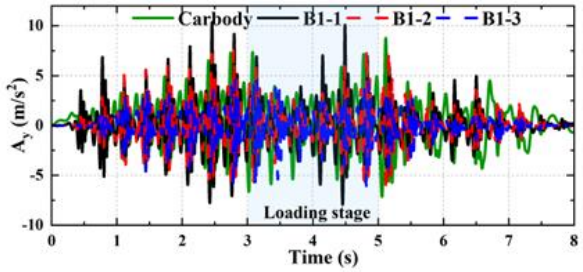

(h1) Lateral acceleration of the car body and bogies

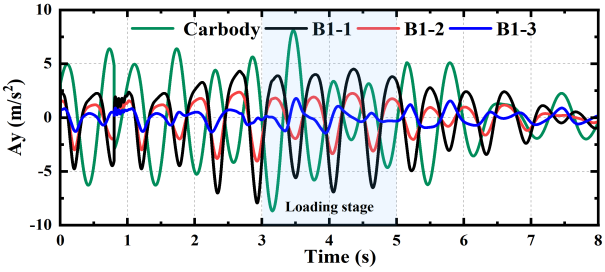

(h2) Lateral acceleration of the car body and bogies

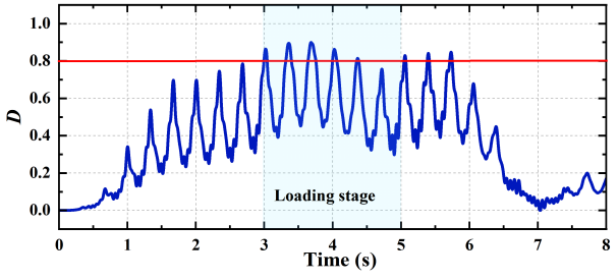

(i1) Overturning coefficient

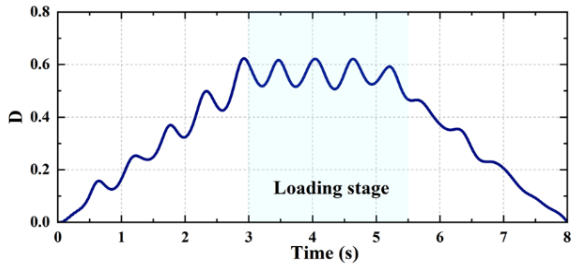

(i2) Overturning coefficient

Fig. 17 Dynamic response of the head car and bogies of two loading methods in Scenario A

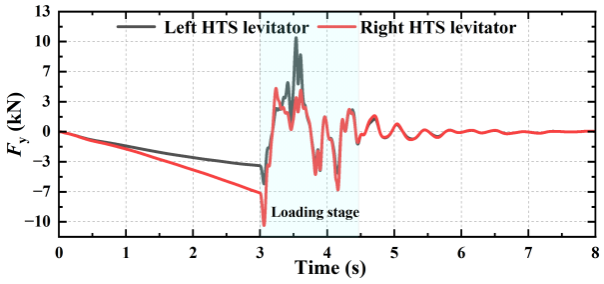

(a1) Guidance force

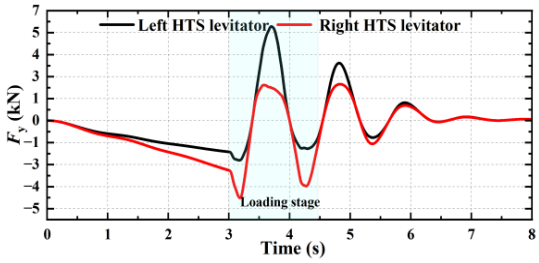

(a2) Guidance force

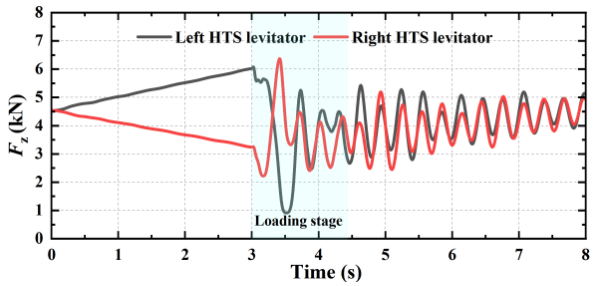

(b1) Levitation force

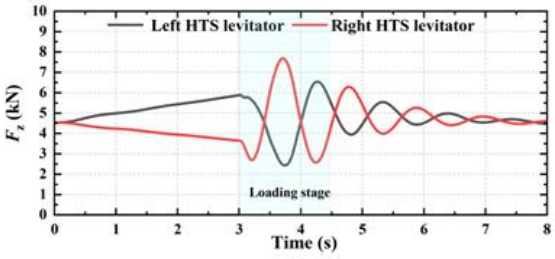

(b2) Levitation force

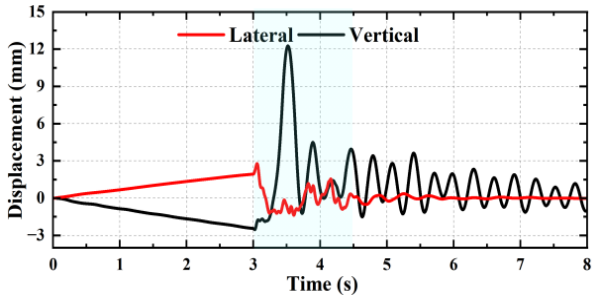

(c1) Vertical and lateral displacement

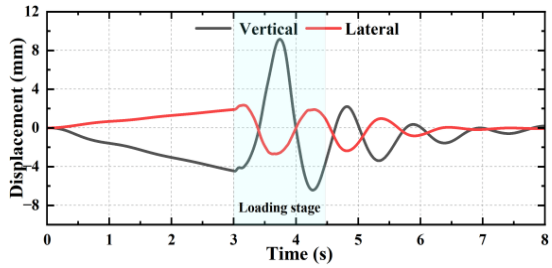

(c2) Vertical and lateral displacement

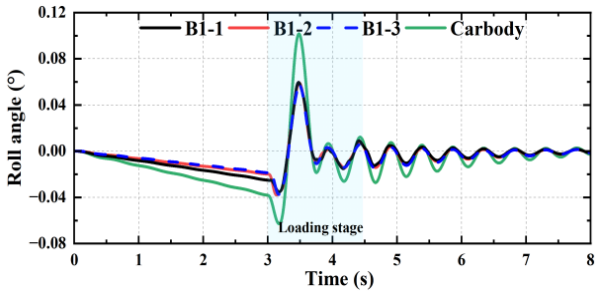

(d1) Yaw angle of the car body and bogies

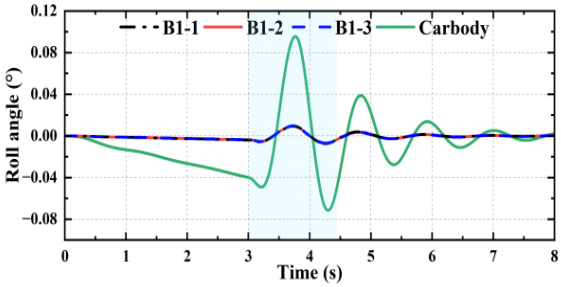

(d2) Vertical and lateral displacement

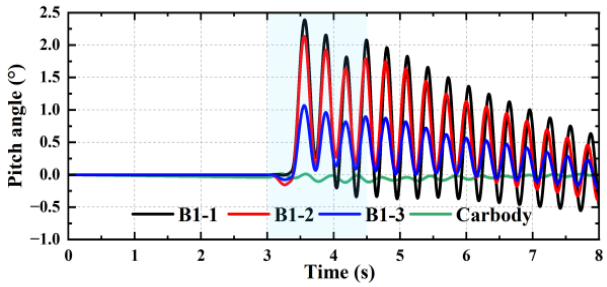

(e1) Pitch angle of the car body and bogies

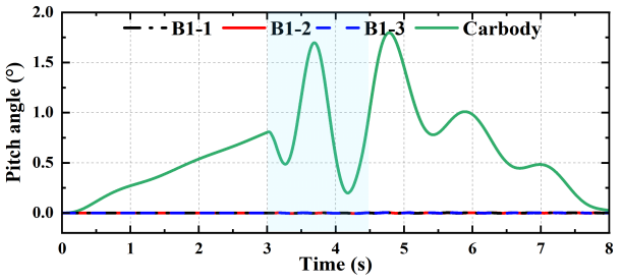

(e2) Pitch angle of the car body and bogies

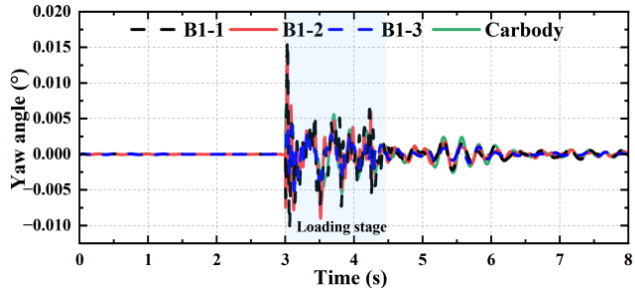

(f1) Roll angle of the car body and bogies

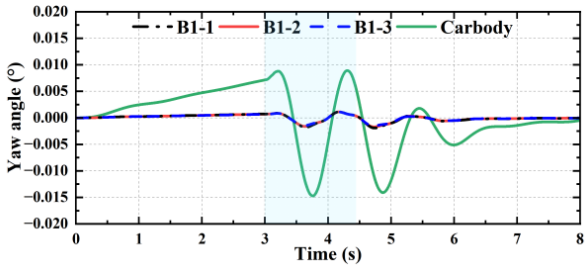

(f2) Roll angle of the car body and bogies

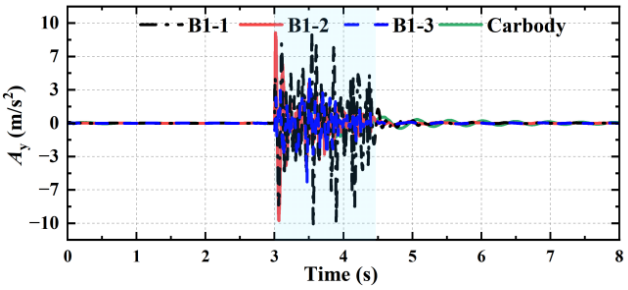

(g1) Vertical acceleration of the car body and bogies

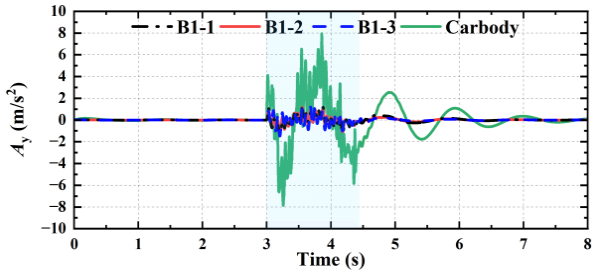

(g2) Vertical acceleration of the car body and bogies

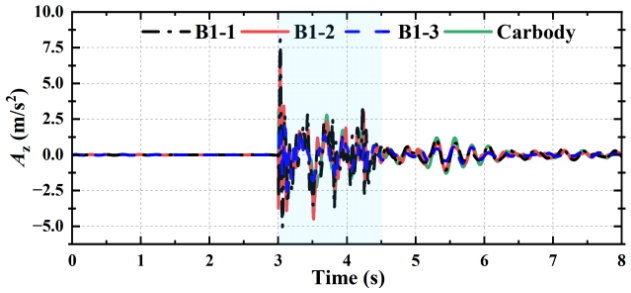

(h1) Lateral acceleration of the car body and bogies

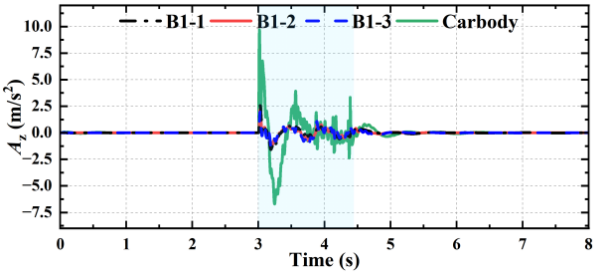

(h2) Lateral acceleration of the car body and bogies

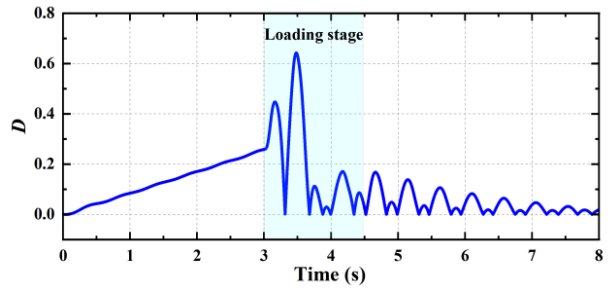

(i1) Overturning coefficient

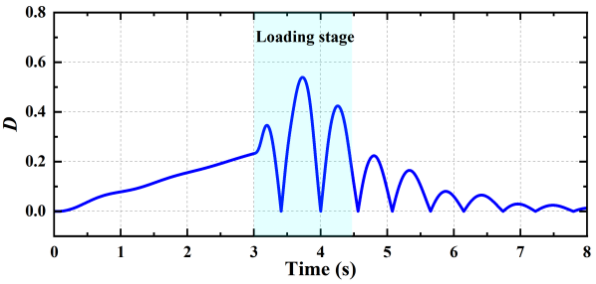

(i2) Overturning coefficient

Fig. 18 Dynamic response of the head car and bogies of two loading methods in Scenario B

force ranges from 0 to -12 kN, while the levitation force exhibits a wider fluctuation range, reaching a maximum of 33 kN. The amplitude variations of the levitation force are more pronounced than those of the guidance force, particularly during the aerodynamic load phase. The vertical displacement of the left levitator surpasses its lateral displacement, reaching a maximum of 10 mm, indicating a necessity for focus on and enhancement of vertical safety performance. Figures 17 (a2), (b2), and (c2) exhibit analogous patterns, characterized primarily by a notably decreased oscillation frequency and diminished amplitude values. Figures 17 (d), (e), and (f) depict the rotational angles of the B1-1 bogie across three axes. The annotations (d1), (e1), and (f1) demonstrate that the angles for B1-1, B1-2, and B1-3 exceed those of the car body, with B1-1 exhibiting the highest pitch angle of 2.2° and the lowest yaw angle of 0.03°. Figures 17 (d2), (e2), and (f2) illustrate that the rotational angles of the car body significantly surpass those of the bogie. The whole-vehicle loading method neglects aerodynamic loads in the bogies area, leading to reduced dynamic responses. Figures 17 (g) and (h) illustrate the variations in lateral and vertical vibration acceleration for the car body and bogie, with both exhibiting fluctuations within ±10 m/s². The findings indicate that the bogie's dynamic response decreases with increased overall loading, while the greater mass of the car body leads to reduced oscillation frequencies across all dynamic parameters. Figure 17 (i1)

demonstrates the variations in the overturning coefficient *D*, which rises with the introduction of aerodynamic loads. Under partitioned independent loading conditions, *D* exceeds 0.8, indicating a significant risk of train overturning and necessitating safety optimization measures. Conversely, Fig. 17 (i2) illustrates that the alterations stay within acceptable limits, suggesting that the whole-vehicle loading method produces safer outcomes; however, this may lead researchers to undervalue the significance of safety measures.

Figure 18 presents the dynamic response in Scenario B, comparing the responses associated with zone-loading (a1-i1) and whole-vehicle loading (a2-i2) methods. Whole-vehicle loading, akin to Scenario A, yields smaller parameter values and decreases the frequency of value changes. From 0 to 3 seconds, the aerodynamic loads increase gradually, resulting in linear changes in all parameters. Fluctuations commence after 3 seconds, with amplitudes reaching their peak around 3.6 seconds. After 4.4 seconds, the oscillations gradually diminish as the aerodynamic loads are released. The guidance force exhibits a variation of ±10 kN, while the vertical displacement of the levitator reaches a maximum of 12 mm during load application. The pitch angle of the B1-1 bogie attains a maximum of 2.5°, indicating a notable lift effect. The overturning coefficients depicted in Figures (i1) and (i2) remain within acceptable limits, with peak values recorded during the train's transit through the gap in the windbreak wall.

5. CONCLUSIONS

This study examines the influence and role of the suspension bogies system in the numerical prediction of the dynamic response of HTS maglev trains subjected to crosswind conditions. The primary findings are summarized as follows:

(1) In Scenario A, the risk of train overturning is greater than in Scenario B. The independent partitioning and loading of aerodynamic forces on the car body and bogies significantly affect the numerical predictions of dynamic responses and crosswind safety for the HTS maglev train.

(2) In Scenarios A and B, the head car is subject to unsteady aerodynamic forces characterized by significant mean values, substantial amplitudes, and complex frequency components, which require careful consideration of its safety. The B1-1 bogie exhibits the most pronounced unsteady aerodynamic characteristics and significantly influences the high-frequency oscillations of the aerodynamic loads on the car body. A focused approach is necessary for ensuring the operational stability and safety of the head car. This begins with the optimization of the B1-1 bogie design to reduce the effects of aerodynamic loads, and is followed by the incorporation of vibration-damping features.

(3) In Scenario A, safety considerations regarding crosswinds must incorporate low frequencies in the range of 1-5 Hz, as well as a broader spectrum of higher frequencies exceeding 10 Hz, which influence the stability of the vehicle system. The middle and tail cars demonstrate reduced unsteady load fluctuations, emphasizing the impact of low-frequency vibrations on safety.

(4) In both Scenario A and B, the omission of the partitioned independent loading results in an underestimation of the levitation force, guidance force, displacement of the HTS levitator, and the dynamic response of the bogies, as well as a reduction in the frequency of these parameters. It is advisable to implement the partition loading strategy to evaluate the crosswind safety and dynamic response of high-speed HTS maglev trains.

ACKNOWLEDGMENTS

This work was partially supported by the National Natural Science Foundation of China (U24B20125), the S&T Program of Hebei (23567602H), and the China National Railway Group Science and Technology Program (K2024T005).

CONFLICT OF INTEREST

The author(s) declared no potential conflicts of interest with respect to the research, authorship, and/or publication of this article.

AUTHORS CONTRIBUTION

Z. P. Li: Conceptualization, Data curation, Formal analysis, Investigation, Methodology, Software, Supervision, Visualization, Writing – original draft, Writing – review & editing; **X. F. Wang:** Data curation, Software, Validation; **Y. M. Pan:** Data curation, Writing – review & editing; **Y. Ding:** Software, Writing – review & editing; **Z. G. Deng:** Funding acquisition, Project administration, Resources, Writing – review & editing; **P. F. Liu:** Funding acquisition, Project administration, Resources, Writing – review & editing.

REFERENCES

Baker, C. (2009). The flow around high speed trains. *Journal of Wind Engineering and Industrial Aerodynamics*, *98*(6–7), 277–298. https://doi.org/10.1016/j.jweia.2009.11.002

Baker, C. J. (2014). A review of train aerodynamics Part 1 – Fundamentals. *The Aeronautical Journal*, *118*(1201), 201–228. https://doi.org/10.1017/s000192400000909x

Baker, C., Jones, J., Lopez-Calleja, F., & Munday, J. (2004). Measurements of the cross wind forces on trains. *Journal of Wind Engineering and Industrial Aerodynamics*, *92*(7–8), 547–563. https://doi.org/10.1016/j.jweia.2004.03.002

Chen, Z., Liu, T., Yan, C., Yu, M., Guo, Z., & Wang, T. (2019). Numerical simulation and comparison of the slipstreams of trains with different nose lengths under crosswind. *Journal of Wind Engineering and*

Industrial Aerodynamics, *190*, 256–272. https://doi.org/10.1016/j.jweia.2019.05.005

Deng, Z., Zhang, W., Zheng, J., Ren, Y., Jiang, D., Zheng, X., Zhang, J., Gao, P., Lin, Q., Song, B., & Deng, C. (2016). A high-temperature superconducting maglev ring test line developed in Chengdu, China. *IEEE Transactions on Applied Superconductivity*, *26*(6), 1–8. https://doi.org/10.1109/tasc.2016.2555921

Ding, S., Liu, J., and Chen, D. (2023). Aerodynamic design of the 600 km/h high-speed maglev transportation system. *Journal of Experiments in Fluid Mechanics*, *37*(1), 1-8. https://doi.org/10.11729/syltlx20220131

Dorigatti, F., Sterling, M., Baker, C., & Quinn, A. (2015). Crosswind effects on the stability of a model passenger train—A comparison of static and moving experiments. *Journal of Wind Engineering and Industrial Aerodynamics*, *138*, 36–51. https://doi.org/10.1016/j.jweia.2014.11.009

Guo, H., Zhang, K., Xu, G., & Niu, J. (2023). Unsteady aerodynamic behaviour of high-speed maglev trains during plate braking in tailwind and headwind opening configurations. *International Journal of Rail Transportation*, 1–18. https://doi.org/10.1080/23248378.2023.2271478

Han, S., Zhang, J., Xiong, X., Ji, P., Zhang, L., Sheridan, J., & Gao, G. (2022). Influence of high-speed maglev train speed on tunnel aerodynamic effects. *Building and Environment*, *223*, 109460. https://doi.org/10.1016/j.buildenv.2022.109460

Hemida, H., & Krajnović, S. (2009). Exploring flow structures around a simplified ICE2 train subjected to a 30° side wind using LES. *Engineering Applications of Computational Fluid Mechanics*, *3*(1), 28–41. https://doi.org/10.1080/19942060.2009.11015252

Hu, X., Li, H., Zhou, X., Zhang, S., Li, H., & Deng, Z. (2024). Modeling and dynamic performance of distributed force in High-Temperature superconducting pinning magnetic levitation. *Physica Scripta*, *99*(10), 105220. https://doi.org/10.1088/1402-4896/ad723a

Huang, Z., Zhou, Z., Chang, N., Chen, Z., & Wang, S. (2024). Aerodynamic features of high-speed maglev trains with different marshaling lengths running on a viaduct under crosswinds. *Computer Modeling in Engineering & Sciences*, *140*(1), 975–996. https://doi.org/10.32604/cmes.2024.047664

Hull, J. R. (2000). Superconducting bearings. *Superconductor Science and Technology*, *13*(2), R1–R15. https://doi.org/10.1088/0953-2048/13/2/201

Kou, L., Deng, Z., Li, H., Wang, L., Rao, Y., & Ke, Z. (2021). A Two-Dimension force model between High-Temperature Superconducting Bulk YBACUO and Halbach-Type Permanent Magnet guideway. *IEEE Transactions on Applied Superconductivity*, *31*(4), 1–8. https://doi.org/10.1109/tasc.2021.3064274

Krajnović, S., Ringqvist, P., Nakade, K., & Basara, B. (2012). Large eddy simulation of the flow around a simplified train moving through a crosswind flow. *Journal of Wind Engineering and Industrial Aerodynamics*, *110*, 86–99. https://doi.org/10.1016/j.jweia.2012.07.001

Li, T., Qin, D., & Zhang, J. (2019). Effect of RANS turbulence model on aerodynamic behavior of trains in crosswind. *Chinese Journal of Mechanical Engineering*, *32*(1). https://doi.org/10.1186/s10033-019-0402-2

Li, T., Zhang, J., & Zhang, W. (2012). Co-simulation of high-speed train fluid-structure interaction dynamics in crosswinds. *Journal of Vibrational Engineering & Technologies*. https://en.cnki.com.cn/Article_en/CJFDTOTAL-ZDGC201202007.htm

Li, Z., Wang, X., Ding, Y., Wang, J., Liu, P., & Deng, Z. (2023). Study on the dynamics characteristics of hts maglev train considering the aerodynamic loads under crosswinds. *Sustainability*, *15*(23), 16511. https://doi.org/10.3390/su152316511

Lin, T. T., Yang, M. Z., Zhang, L., Wang, T. T., Liu, D. R., Tao, Y., & Zhong, S. (2024). Influence of the suspension gap on the wake characteristics of a 600 km/h superconducting maglev train. *Physics of Fluids*, *36*(2). https://doi.org/10.1063/5.0190742

Liu, D., Liang, X., Zhou, W., Zhang, L., Lu, Z., & Zhong, M. (2022). Contributions of bogie aerodynamic loads to the crosswind safety of a high-speed train. *Journal of Wind Engineering and Industrial Aerodynamics*, *228*, 105082. https://doi.org/10.1016/j.jweia.2022.105082

Liu, J., Yu, M., Zhang, J., & Zhang, W. (2011) Study on running safety of high-speed train under crosswind by large eddy simulation. *Journal of the China Railway Society*. https://en.cnki.com.cn/Article_en/CJFDTOTAL-TDXB201104005.htm

Lv, D., Liu, Y., Zheng, Q., Zhang, L., & Niu, J. (2023). Unsteady aerodynamic characteristics and dynamic performance of high-speed trains during plate braking under crosswind. *Nonlinear Dynamics*, *111*(15), 13919–13938. https://doi.org/10.1007/s11071-023-08608-2

Mattos, L. S., Rodriguez, E., Costa, F., Sotelo, G. G., De Andrade, R., & Stephan, R. M. (2016). MagLev-cobra operational tests. *IEEE Transactions on Applied Superconductivity*, *26*(3), 1–4. https://doi.org/10.1109/tasc.2016.2524473

Meng, S., Zhou, D., & Tan, C. (2022). The effect of concave size on the aerodynamics of a Maglev train. *Journal of Bionic Engineering*, *19*(3), 709–723. https://doi.org/10.1007/s42235-022-00158-4

Munoz-Paniagua, J., García, J., & Lehugeur, B. (2017). Evaluation of RANS, SAS and IDDES models for the simulation of the flow around a high-speed train subjected to crosswind. *Journal of Wind Engineering and Industrial Aerodynamics*, *171*, 50–66. https://doi.org/10.1016/j.jweia.2017.09.006

Niu, J., Zhou, D., & Wang, Y. (2018). Numerical comparison of aerodynamic performance of stationary and moving trains with or without windbreak wall under crosswind. *Journal of Wind Engineering and Industrial Aerodynamics*, *182*, 1–15. https://doi.org/10.1016/j.jweia.2018.09.011

Sawada, K. (2009). Outlook of the superconducting Maglev. *Proceedings of the IEEE*, *97*(11), 1881–1885. https://doi.org/10.1109/jproc.2009.2030246

Sotelo, G. G., De Oliveira, R. a. H., Costa, F. S., Dias, D. H. N., De Andrade, R., & Stephan, R. M. (2015). A full scale Superconducting Magnetic Levitation (MaGLEV) vehicle operational line. *IEEE Transactions on Applied Superconductivity*, *25*(3), 1–5. https://doi.org/10.1109/tasc.2014.2371432

Suzuki, M., Tanemoto, K., & Maeda, T. (2003). Aerodynamic Characteristics of Train/Vehicles under Cross Winds. Journal of Web Engineering, 89, 505–508. http://ci.nii.ac.jp/naid/10007252333

Tian, H. (2019). Review of research on high-speed railway aerodynamics in China. *Transportation Safety and Environment*, *1*(1), 1–21. https://doi.org/10.1093/tse/tdz014

Tian, X., Xiang, H., Chen, X., & Li, Y. (2023). Dynamic response analysis of high-speed maglev train-guideway system under crosswinds. *Journal of Central South University*, *30*(8), 2757–2771. https://doi.org/10.1007/s11771-023-5403-8

Wang, J., Wang, S., Zeng, Y., Huang, H., Luo, F., Xu, Z., Tang, Q., Lin, G., Zhang, C., Ren, Z., Zhao, G., Zhu, D., Wang, S., Jiang, H., Zhu, M., Deng, C., Hu, P., Li, C., Liu, F., Lian, J., Wang, X., Wang, L., Shen, X., Dong, X. (2002). The first man-loading high temperature superconducting Maglev test vehicle in the world. *Physica C Superconductivity*, *378–381*, 809–814. https://doi.org/10.1016/s0921-4534(02)01548-4

Wang, J., Wang, S., Deng, C., Zheng, J., Song, H., He, Q., Zeng, Y., Deng, Z., Li, J., Ma, G., Jing, H., Huang, Y., Zhang, J., Lu, Y., Liu, L., Wang, L., Zhang, J., Zhang, L., Liu, M., Qin, Y., Zhang, Y. (2007). Laboratory-Scale high temperature Superconducting Maglev launch system. *IEEE Transactions on Applied Superconductivity*, *17*(2), 2091–2094. https://doi.org/10.1109/tasc.2007.898367

Wang, S., Li, H., Wang, L., Huang, H., Deng, Z., & Zhang, W. (2021). Suspension parameters optimization of HTS maglev under random vibration. *IEEE Transactions on Applied Superconductivity*, *31*(8), 1–4. https://doi.org/10.1109/tasc.2021.3094427

Wang, S., Wang, J., Wang, X., Ren, Z., Zeng, Y., Deng, C., Jiang, H., Zhu, M., Lin, G., Xu, Z., Zhu, D., & Song, H. (2003). The man-loading high-temperature superconducting maglev test vehicle. *IEEE Transactions on Applied Superconductivity*, *13*(2), 2134–2137. https://doi.org/10.1109/tasc.2003.813017

Wang, X., Hu, X., Wang, J., Wang, L., Li, H., Deng, Z., & Zhang, W. (2023). Safety analysis of high temperature superconducting maglev train considering the aerodynamic loads under crosswinds. *Proceedings of the Institution of Mechanical Engineers Part C Journal of Mechanical Engineering Science*, *237*(10), 2279–2290. https://doi.org/10.1177/09544062221140033

Werfel, F. N., Floegel-Delor, U., Rothfeld, R., Riedel, T., Goebel, B., Wippich, D., & Schirrmeister, P. (2011). Superconductor bearings, flywheels and transportation. *Superconductor Science and Technology*, *25*(1), 014007. https://doi.org/10.1088/0953-2048/25/1/014007

Yu, M. (2012). Unsteady Aerodynamic Loads of High-speed Trains under Stochastic Winds. *Journal of Mechanical Engineering*, *48*(20), 113. https://doi.org/10.3901/jme.2012.20.113

Zhang, L. (2016). Unsteady aerodynamic characteristics and safety of high-speed trains under crosswinds. *Journal of Mechanical Engineering*, *52*(6), 124. https://doi.org/10.3901/jme.2016.06.124

Zhang, W. (2012). Dynamic performance of high-speed train passing windbreak in crosswind. *Journal of the China Railway Society*. https://en.cnki.com.cn/Article_en/CJFDTOTAL-TDXB201207008.htm

Zhang, W. (2013). Study on characteristics of unsteady aerodynamic loads of a high-speed train under crosswinds by large eddy simulation. *Journal of the China Railway Society*. https://en.cnki.com.cn/Article_en/CJFDTOTAL-TDXB201306004.htm

Zhou, P., Qin, D., Zhang, J., & Li, T. (2021). Aerodynamic characteristics of the evacuated tube maglev train considering the suspension gap. *International Journal of Rail Transportation*, *10*(2), 195–215. https://doi.org/10.1080/23248378.2021.1885514